Chapter 9
Impact Comminution in Jet Mills

Alexander Strobel, Benedikt Köninger, Stefan Romeis, Karl-Ernst Wirth, and Wolfgang Peukert

Abstract Modelling the comminution in jet mills with respect to the complex two-phase flow and the dynamic process behaviour is still a challenging task. The processed solids pass through several stages in the mill: The comminution process in the lower part, the pneumatic transport towards the classifier in the middle section, and the classification step at the top. In this contribution, the grinding kinetics and process behaviour during quasi-batch and fed-batch operational mode for different holdups, classifier speeds, and particle sizes are examined in detail. A previously developed method using well-characterized aluminium particle probes to access the stressing conditions is adapted for application in the investigated jet mill: The relative particle impact velocity is linked to the geometric changes of the particles upon impact. A high number of impact events happen in the mill, while at the same time, the average particle velocity is comparatively low. Besides the stressing conditions, breakage probabilities for the used glass beads are determined by single particle impact experiments and described by the model of Vogel and Peukert. Solids concentration measurements and high-speed imaging reveal the formation of particle clusters at the classifier and its periphery. These clusters have a massive impact on the classification step itself: Fine particles are trapped inside the clusters and are not discharged. Based on an adaption of the breakage model, and using the mean relative particle impact velocity determined by the particle probes, a model for the product mass flow is introduced.

Nomenclature

$(1-\varepsilon)$	Solid volume fraction [–]
$(1-\varepsilon)_r$	Solid volume fraction at radius r [–]
$(1-\varepsilon)_{jet}$	Solid volume fraction in the jet [–]
a	Particle acceleration [m s^{-2}]

A. Strobel · B. Köninger · S. Romeis · K.-E. Wirth · W. Peukert (✉)
Institute of Particle Technology, Friedrich-Alexander-Universität Erlangen-Nürnberg, Erlangen, Germany
e-mail: wolfgang.peukert@fau.de

S. Heinrich (ed.), *Dynamic Flowsheet Simulation of Solids Processes*,
https://doi.org/10.1007/978-3-030-45168-4_9

A_r	Annulus area of the mill chamber with radius r [m^2]
A	Cross-sectional area of the mill [m^2]
c_w	Drag coefficient [–]
d_0	Nozzle diameter [mm]
E	Young's modulus [Pa]
f_{mat}	Particles' resistance against breakage [kg J^{-1} m^{-1}]
F_W	Drag force [N]
k	Number of impacts [–]
$K^{(1)}(x)$	First Kapur function [s^{-1}]
M	Mass [g]
m_i	Mass of size class i [g]
$m_{i,0}$	Initial mass of size class i [g]
$m_{particle}$	Particle mass [g]
$\dot{m}_i$	Mass flow transported to the classifier [g min^{-1}]
$\dot{m}_{jet}$	Mass flow through a single jet [g min^{-1}]
$\dot{m}_p$	Product mass flow [g min^{-1}]
n	Number of nozzles in the mill [–]
N	Total number of evaluated particles [–]
N_i	Number of particles with I contacts [–]
p	Grinding pressure [bar]
P_B	Breakage probability [–]
P_i	Relative number of particles with i contacts [–]
q_3	Volume-weighted density distribution [m^{-1}]
Q_0	Number-weighted cumulative sum distribution [–]
Q_3	Volume-weighted cumulative sum distribution [–]
r	Radial distance in the milling chamber [m]
R	Outer radius of the milling chamber [m]
R_{cl}	Radius at the outer classifier blade [m]
Re_p	Particle Reynolds number [–]
S	Breakage rate [g min^{-1}]
$SN_{\%}$	Percentage of stressed particles [–]
SN_{stress}	Average contact number per stressed particle [–]
t	Process time [s]
T(x)	Separation efficiency curve [–]
$u_{p,jet}$	Particle velocity in the jet [m s^{-1}]
v	Particle velocity [m s^{-1}]
v_{cl}	Circumferential velocity classifier wheel [m s^{-1}]
v_r	Gas velocity in radial direction [m s^{-1}]
Δv	Relative particle impact velocity [m s^{-1}]
V	Overall volume of all particles [m^3]
V_i	Volume of individual particle [m^3]
$W_{m,min}$	Minimum mass-specific energy input [J kg^{-1}]
$W_{m,kin}$	Mass-specific kinetic energy input [J kg^{-1}]
x	Particle diameter [μm]
$x_{1,2}$	Sauter diameter [μm]

$x_{50,3}$	Mean volume-weighted particle diameter [μm]
x_c	Contact diameter on the particle surface after impact [μm]
x_{cut}	Particle cut size for breakage probability [μm]
x_T	Cut size classifier [μm]
z	Nozzle distance in jet mill [mm]
η	Dynamic viscosity [Pa s]
ν	Poisson ratio [–]
ξ	Product residue [–]
ρ_p	Particle density [kg m^{-3}]
ψ_i	Sphericity of individual particle [–]
ψ	Volume-based mean sphericity [–]

Indices

m	Milling chamber
p	Product
t	Process time
gas	Gas

1 Introduction

Dynamic processes are becoming increasingly important in the field of solid process engineering. The on-demand production, faster product cycles and fluctuating energy supply of renewable (wind or solar) energy are the driving forces of this development. First and foremost, before addressing the modelling of interconnected solids processes, a well-founded understanding of the dynamics of individual unit operations and overall processes is essential [1]. To date, in-depth information on the dynamic behaviour of comminution processes is rare. Modelling of comminution processes is a challenging task [2]: Within the mill, very complex transport phenomena prevail, resulting in mostly unknown stressing conditions. In particular, classifier mills are highly interesting because they involve three coupled unit operations: The comminution in the jet area, the transport to the classification zone, and the classification itself [3]. Although advanced CFD [4–6] or coupled CFD-DEM [2, 7] approaches are available today, the highly turbulent two-phase flows in the mills are far from being understood sufficiently. Other approaches use dynamic model systems for the calculating of closed loop systems [8–10] or population balance methods [11, 12]. The high Reynolds numbers and the steep velocity gradients in combination with the high solids concentrations limit the application of numerical methods [2].

One particular type of classifier mills is the fluidized bed opposed jet mill, which is the method of choice for size reduction of hard, abrasive, and thermosensitive

materials [13]. Through the autogenous comminution by particle-particle impacts induced by the gas jets, a high degree of fragmentation can be achieved for the production of fine powders <10 μm. Since no moving parts for impaction are needed, the comminution proceeds without any wear of the machinery, avoiding also the contamination of the product. The processing of different materials in fluidized bed opposed jet mills is addressed in several different publications [14–18]. These approaches propose empirical models to describe the two-phase flow or just illustrate experimental effects. Other authors describe batch processing in fluidized bed opposed jet mills while global grinding kinetics are employed to model size reduction [19–21]. The complex two-phase flow, the high gas velocities, and the difficulties to directly assess the stressing conditions comprise major challenges. The classification process is studied both experimentally and numerically in stand-alone classifiers, including the fluid mechanics inside the vanes of the rotating classifier wheel [6, 22–28].

The following chapter is dedicated to the study of particle-particle interactions, revealing the overall stressing conditions, and the dynamics of the two-phase flow during non-stationary fine grinding. For this purpose a lab-scale fluidized bed opposed jet mill is investigated in detail: Besides the grinding behaviour during different operational modes, a novel approach for the direct determination of relative particle velocities will be presented. Any comprehensive description of the comminution process requires the knowledge about the materials properties and the materials response to the determined stresses. For this reason the single particle breakage behaviour is studied and analysed by single particle compression and impact tests. The presented observations are then finally used for a model of the product mass flow.

2 Materials and Methods

2.1 Fluidized Bed Opposed Jet Mill

The experiments were performed in a lab-scale fluidized bed opposed jet mill (AFG 100, Hosokawa Alpine AG, Germany). A scheme of the setup is depicted in Fig. 1 [29]. The mill consists of a cylindrical milling chamber (inner diameter of 100 mm). Three Laval nozzles [exit diameters of 1.9 mm (1)] are arranged in a 3D configuration at the bottom of the mill chamber and are directed towards the central focal point. The nozzles are supplied with pressurized air, which leads to a gas flow directed upward towards the classifier wheel (2), whose outer diameter is 50 mm. The mill was operated at a pressure level of 10–20 mbar below ambient conditions. An online laser diffraction system (3) (Insitec, Malvern Panalytical, UK) is installed in the product stream to continuously record the product particle size distributions (PSDs) (sample rate of 1 Hz). Before the online particle size measurement, the product particles are dispersed by a ring nozzle (4). Particle separation after the measurement was ensured by a cyclone and a filter. For the characterization of the material inside

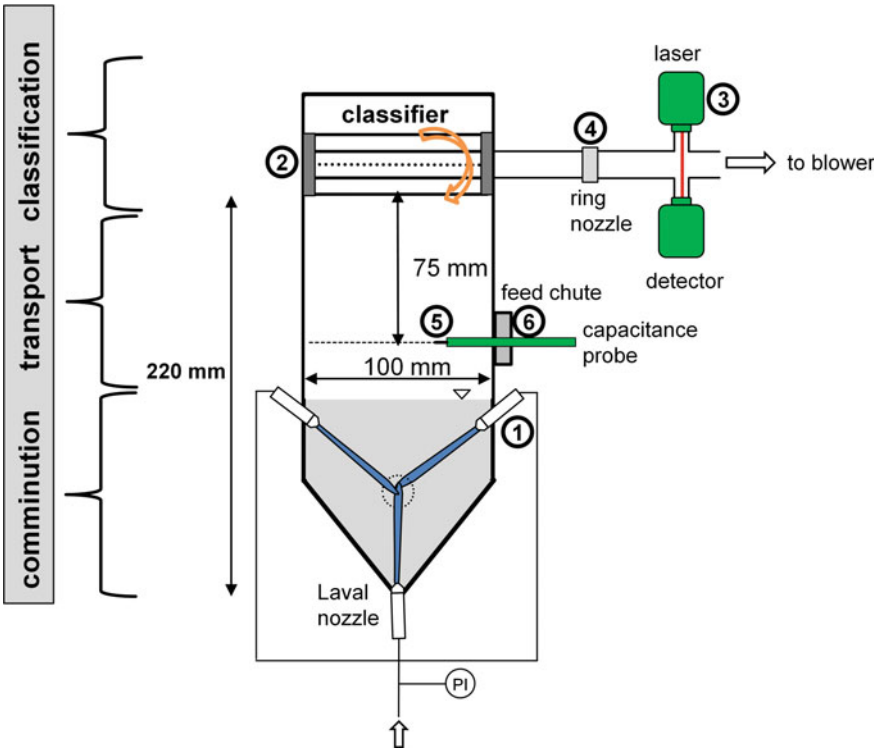

Fig. 1 Scheme of the lab-scale mill AFG 100. (1) Laval nozzles, (2) classifier wheel, (3) online laser diffraction setup, (4) ring nozzle, (5) needle shaped capacitance probes inserted into the custom-made adapter fitted into the original feed chute (6). Adapted from Köninger et al. [29], with kind permission of Elsevier

the mill, the grinding process was interrupted, and the PSD was determined by offline laser diffraction (Mastersizer 2000, Malvern Panalytical, UK). The holdup was determined by weighing.

To measure the solid volume fraction $(1 - \varepsilon)$ in the zone between the upper Laval nozzles and the classifier, capacitance probes (5) were inserted into the milling chamber through a customized measurement adapter which was fitted into the original feed chute (6) (75 mm below the classifier). The capacitance probes are sensitive to changes in the surrounding electromagnetic field caused by the solids: These changes in the capacitance, which are converted to a voltage signal and are further processed by a two-channel amplifier, can be related to the solids concentration surrounding the probes. A calibration procedure is applied [30] to convert the measurement signal to the corresponding solid volume fraction $(1 - \varepsilon)$. The local solid volume fraction $(1 - \varepsilon)_r$ was measured at six different radial positions r, and the data was converted to an overall solid volume fraction as shown by Eq. 1.

$$(1-\varepsilon) = \frac{\sum_{r=0}^{R}(1-\varepsilon)_r \cdot A_r}{A} \quad (1)$$

With A_r being the annulus area of the mill chamber for each position r and A the cross-sectional area of the mill. Measurements close to the walls (r = R) were not possible. The formation of a slight crust on the walls was observed (for the processing of the later introduced limestone). A solids fraction of $1 - \varepsilon = 0.55$ (similar to conditions of a fixed bed) was assumed.

Absolute pressures of up to 6 bar were applied to the gas before entering the grinding chamber via the nozzles, which corresponds to a maximum volumetric gas flow rate of 11.7 m^3h^{-1} through each of the nozzles. The classifier speed was varied between 6000 (circumferential wheel velocity $v_{cl} = 15.7$ m s^{-1}) and 15,000 rpm ($v_{cl} = 39.3$ m s^{-1}). The solids holdup was varied between 100 and 700 g. Within the presented experiments the mill was operated in quasi-batch and fed-batch mode.

To optically access the classifying process, an identical AFG 100 with a customized shaft was used [26, 31]: The original drive shaft of the classifier wheel was replaced by a hollow shaft to visualize the flow through the classifier (customization was done by the Weber group). For further details on the collaboration, please refer to the joint publication [31]. The hollow shaft and the original feed chute are placed on opposing sites in the milling chamber, allowing optical access to the fluid and particle flow through the classifier wheel and the surrounding area, while the original geometries are maintained. Imaging was performed by placing a high-speed camera (Keyence VW-600M, 640 × 240 or 320 × 240 pixels resolution, 8000 or 12,000 fps) in front of a window located in the original feed chute. Illumination is realized with a tripod lamp across the ceiling window to prevent any light reflections. For further details, we refer to Stender et al. [26] and Spötter et al. [32].

2.1.1 Quasi-Batch Experiments

For quasi-batch grinding experiments, the mill was only operated with the initially given amount of solids. Besides product-sized material being discharged during the process, the holdup did not change by more than 15% (for the processing of soda-lime glass beads). The process was interrupted at predefined time intervals to measure the powder mass in the milling chamber and its PSD. Thus, by simple mass balancing, the product mass flow rate was calculated. For this purpose, the complete holdup was removed from the mill and thoroughly mixed. Three individual samples were taken for size analysis (Mastersizer 2000, Malvern Panalytical, UK). All experiments were repeated three times, and mean values and standard deviations were calculated accordingly. Changes in the sampling intervals did not show a significant influence on the obtained results.

2.1.2 Fed-Batch Experiments

During quasi-batch experiments, the holdup and the PSD in the milling chamber are changing simultaneously. Therefore, the influences of individual parameters on the process cannot be differentiated. To minimize the influence of the changing holdup, fed-batch experiments were performed: The process is interrupted in fixed intervals to stock up the holdup with the feed material. Within the first 5 min of operation, an interval of 1 min was chosen, followed by a 5 min interval for the remaining process time. Sampling was performed according to the protocol given above.

2.2 Fluidized Bed with Secondary Gas Injection

For some case studies, a lab-scale fluidized bed [33, 34] (inner diameter of 94 mm, circulation zone height of 570 mm) with secondary gas injection was used. Fluidization gas velocity was set to 2.4 cm s^{-1}. A sintered metal plate at the bottom of the bed was used to ensure a homogeneously distribution of the gas. For particle separation, a cyclone and a filter are installed at the top. The diameter d_0 of the used nozzles was 2 mm. A single nozzle setup and a two-opposing nozzle setup were investigated. The distance to the focal point of the opposing nozzles was 42 mm. The jet velocity was set to 200 m s^{-1} (velocity at the nozzle threat). Sampling was performed after intervals of 10 min by dismantling the lower segment of the fluidized bed: The solid was manually mixed and samples were taken at three different spots and merged.

2.3 Material

2.3.1 Soda-Lime Glass Beads

Spherical soda-lime glass beads (Silibeads®, Type S) by Sigmund Lindner (Germany) were used as model particles. In comparison to other investigated materials like talc [35], hydrargillite [9, 19] or ethenzamide [20, 36] the glass beads have distinct advantages for the chosen application: They show superior mechanical properties (Mohs hardness ≥6, Young's modulus E = 63 GPa, [37]) and thus show rather slow breakage. By purposely slowing down the comminution process, the dynamic changes of the process can be observed in greater detail. The density of the beads was 2500 kg m^{-3}.

For the investigation of the grinding dynamics and kinetics, as-received feed fractions with Sauter diameters $x_{1,2}$ of 61, 93, and 127 µm and corresponding spans $((x_{90,3} - x_{10,3})/x_{50,3})$ of 0.71, 0.68 and 0.64, respectively, were used. The corresponding PSDs are given in Fig. 2a together with an SEM image of one of the feed fractions (Fig. 2b). From the SEM images, the sphericity ψ_i of the individual particles is calculated according to Eq. 2:

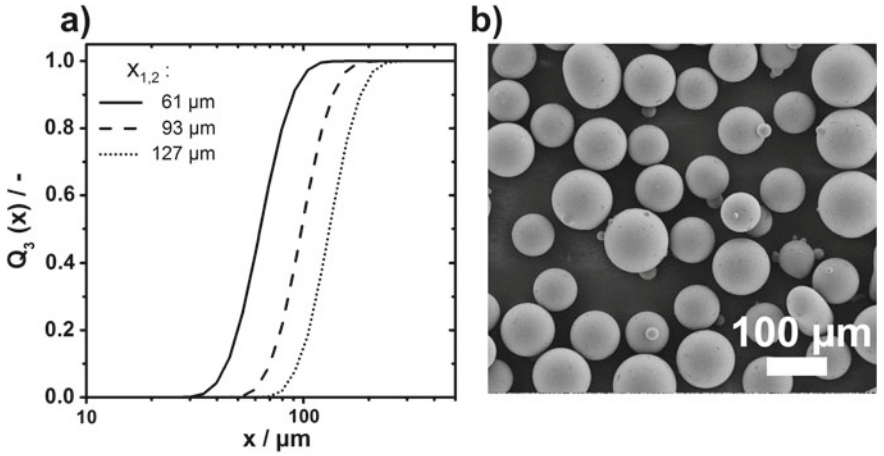

Fig. 2 PSDs of the as-received soda-lime glass beads. Sauter diameters of the fractions are 61, 93, and 127 µm (**a**). **b** SEM-image of the $x_{1,2} = 93$ µm feed material. Adapted from Köninger et al. [29], with kind permission of Elsevier

$$\psi_i = \frac{2\sqrt{\pi \cdot area}}{perimeter} \tag{2}$$

From the perimeter of each analysed particle, an equivalent diameter was determined, which was further used for calculating the volume V_i of the corresponding equivalent sphere. Subsequently, the volume-based mean sphericity is calculated according to Eq. 3:

$$\psi = \sum \psi_i \frac{V_i}{V} \tag{3}$$

For the evaluation of the relative particle impact velocities, the feed material from Sigmund Lindner was narrowed by sieving, resulting in a particle fraction with an $x_{50,3}$ and a span of 55.1 µm and 0.71, respectively (Mastersizer 2000, Malvern Panalytical, UK). The distribution is displayed in Fig. 3a.

2.3.2 Aluminium Probe Particles

To assess the relative particle impact velocities, spherical aluminium particles (TLS Technik & Spezialpulver, Germany) were used together with glass beads as feed material; the size distribution was likewise adjusted by sieving. The resulting PSD is displayed in Fig. 3a. The $x_{50,3}$ value for the aluminium spheres was 53.8 µm (span 0.87). An SEM image of the particles is given in Fig. 3b. The density was 2.70 g/cm^3

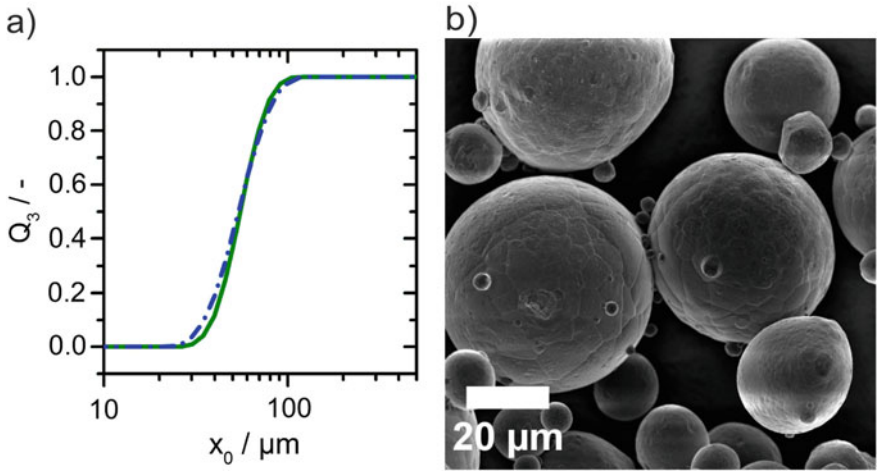

Fig. 3 **a** PSDs of the narrowed glass (blue, dashed-dotted) and aluminium (green, solid) fraction. **b** SEM image of aluminium spheres. Adapted from Strobel et al. [33], with kind permission of Elsevier

as measured by helium pycnometry (Accupyc, Micromeritics, USA). The aluminium particles were later mixed with the glass beads (1:19 m/m) for the experiments.

2.3.3 Limestone

For the presented experiments targeting the particle transport and the separation at the classifier, irregular limestone particles (Saxolith, SH-Minerals GmbH, Germany) were used. Compared to the glass beads, the PSD is rather broad, i.e. $x_{50,3}$ and $x_{1,2}$ of 67 µm and 15 µm, respectively, have been measured. The density of the particles is 2700 kg m^{-3}. By pressure drop measurements, a minimum fluidization velocity of 0.007 m s^{-1} was determined.

2.4 Characterization Methods

2.4.1 Scanning Electron Microscopy (SEM)

Scanning electron microscopy was performed with a GeminiSEM 500 (Carl Zeiss Jena, Germany). Both, a secondary electron detector and a through-the-lens detector (Inlens) were used for imaging. The acceleration voltage was set to 2 kV.

2.4.2 Offline Laser Diffraction

A Mastersizer 2000 equipped with the wet dispersing unit hydro 2000S (Malvern Panalytical, UK) with water as dispersant was used for offline particle size measurements. Loose agglomerates were broken by ultrasound. All samples were measured 5 times with an accumulation time of 10 s, the average values are reported.

2.4.3 Single Particle Impact Testing

Single particle breakage and deformation behaviour was characterized by impacting individual particles using the Schönert breakage device and a custom-build low-pressure impact device. A detailed description of the Schönert device can be found in the work of Meier et al. [38]. In brief, the particles are fed by a vibrational channel onto the centre of a horizontal rotor disc. The rotating disc accelerates the particles towards an outer tooth-shaped ring. The shape of the outer ring ensures an angle of 90° upon impact. To minimize friction, the whole device can be operated at reduced pressure. From the rotational speed of the disc, the impact velocity is then calculated.

A scheme of a second low-pressure impact device is depicted in Fig. 4. The attached vacuum pump reaches pressures down to 20 mbar. For speed regulation, the pressure inside the impact chamber is varied. Impact distance and angle can be changed. Particle velocity was measured by particle image velocimetry (PIV). The PIV system (ILA GmbH, Jülich, Germany) consisted of two pulsed Nd–YAG lasers, a fast high resolution recording CCD camera (PCO2000, 2048 × 2048 pixels) and a synchronizer. The time step between two consecutive images was 4 µs. From the know time step and the travelled particle distance, the velocity prior to the impact is calculated.

From the PSDs prior and after impacting the breakage probability P_B can be calculated. On basis of the well-known Vogel and Peukert model [39], the breakage probabilities P_B and changes in mass for individual size classes (index i) were determined. A simplified calculation according to Eq. 4 was used for the evaluation. Similar to sieve analysis, a nominal cut size x_{cut} is used. The evaluation is based on the assumption that the breakage probability for a given impact velocity is the same for all particles belonging to the identical size class. After impacting the material, the change in mass of the fraction above the cut size is then related to the initial mass before any impact took place (k = 0).

$$P_B = \frac{\Delta m_i}{m_{i,0}} = \frac{Q_3(x_{cut}) - Q_{3,k=0}(x_{cut})}{1 - Q_3(x_{cut})} \tag{4}$$

Impact experiments in a third custom-build impact device were performed to identify the yield strength and the tangent modulus for the material's model needed in

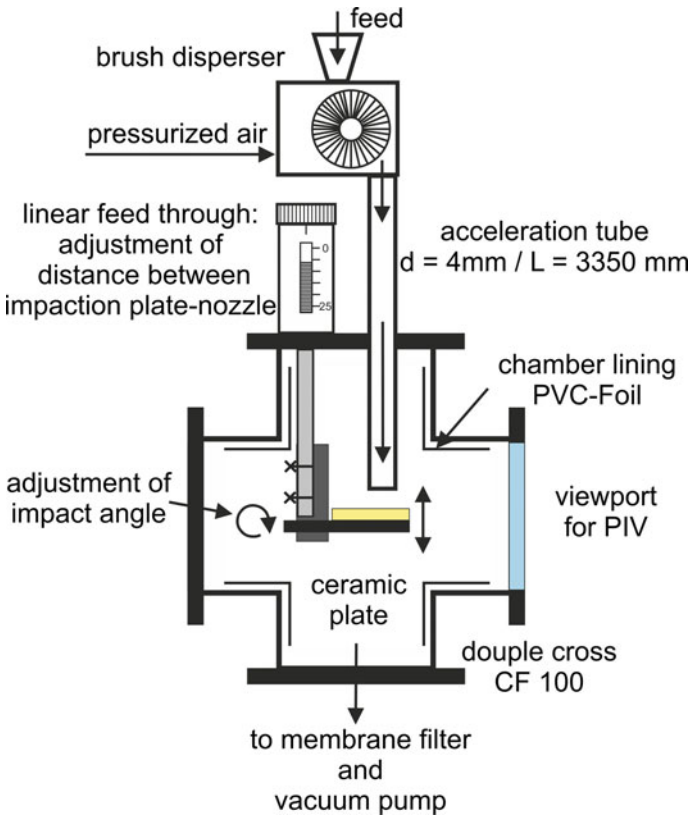

Fig. 4 Low-pressure particle impact device

the finite element calculations. Therefore, aluminium spheres with an initial diameter of 6 mm (Umarex, Germany) were accelerated towards a rectangular steel plate (150 mm × 150 mm × 20 mm, length × width × height) using pressurized air. Before impact, the velocity of the particles was measured by two light barriers installed in close distance to the impact plate. The size of the formed spherical contact area (minimum Feret diameter) on the surface of the particles was related to the particle size ratio x_c/x. By using a scale paper placed in the plain of the contact, the minimum Feret diameter of the contact area was determined from photographic images. Therefore, the waist diameter equals the initial particle diameter. No changes in the waist diameter were detected within the evaluated impact velocity range.

2.4.4 Finite Element Modelling (FEM)

Simulations of the particle-particle as well as the particle-wall impacts were performed using the software package Ansys V.17.2 (Ansys Inc., USA). A 3D model was used for all simulations. To access the mechanical properties of the used aluminium spheres for simulating the particle-particle impacts in the jet mill, a first set of simulations for the impact of an aluminium sphere (6 mm) on a steel plate (90° angle) were performed. Yield strength and tangent modulus of the aluminium sphere were fitted until a sufficient match of the simulated and experimentally observed geometries was found. Young's moduli and Poisson ratios are listed in Table 1.

Dimensions of the sphere and the impact plate were chosen according to the experimental setup. The number of nodes and eight-node quadratic quadrilateral elements used in the simulation is given in Table 2. The coefficient of static friction was determined to be 0.44 by using the impact plate and the contact surface of an impacted 6 mm sphere (impact velocity of 60 m s^{-1}) in an inclined plane experiment (average of 20 repetitions).

In the second step, the particle-particle impact between a glass and an aluminium sphere along the line connecting their gravity centres was simulated. Dimensions were set according to the used feed materials. The inclined plane experiment of a glass bead layer on aluminium gave a static friction coefficient of 0.28.

Table 1 Mechanical properties used for the simulation

	E/GPa	ν/–
Aluminium sphere [40]	68	0.34
Steel plate	200	0.30
Glass sphere	63	0.20 [41]

Table 2 Number of nodes and eight-node quadratic quadrilateral elements of the simulated geometries

	Nodes	Elements
Impact sphere-plate		
Aluminium sphere	720,000	530,000
Impact plate	145,000	105,000
Impact sphere-sphere		
Glass sphere	143,000	103,000
Aluminium sphere	700,000	517,000

3 Results and Discussion

3.1 Dynamics of Quasi-Batch Comminution

3.1.1 Size Evolution and Morphology

The generation of a fine product of a few µm in size requires a sufficiently high classifier speed. The classifier speed was set to 12,500 rpm, which corresponds to a circumferential classifier velocity v_{cl} of 32.7 m s^{-1} and a nominal cut size x_T = 4.3 µm at the vanes of the classifier wheel [30].

In Fig. 5 changes in the particle size and sphericity during quasi-batch grinding are depicted. The particle sizes $x_{1,2}$ and $x_{50,3}$ decrease with time (Fig. 5a); within the first 80 s an almost linear trend is observed. However, after the first 80 s, the Sauter diameter $x_{1,2}$ decreases significantly faster than x_{50}. This observation is attributed to a slow initial breakage of the feed particles, while the breakage of the fragments is accelerated. The fragments show a higher specific surface area and, in consequence, cause the observed change of $x_{1,2}$. A similar trend is observed for the volume-based mean sphericity ψ: Up to a processing time of 80 s, the sphericity decreases strongly. After this period, the overall morphology and with it, the sphericity of the broken fraction stays almost constant. The SEM images in Fig. 5b confirm that for short

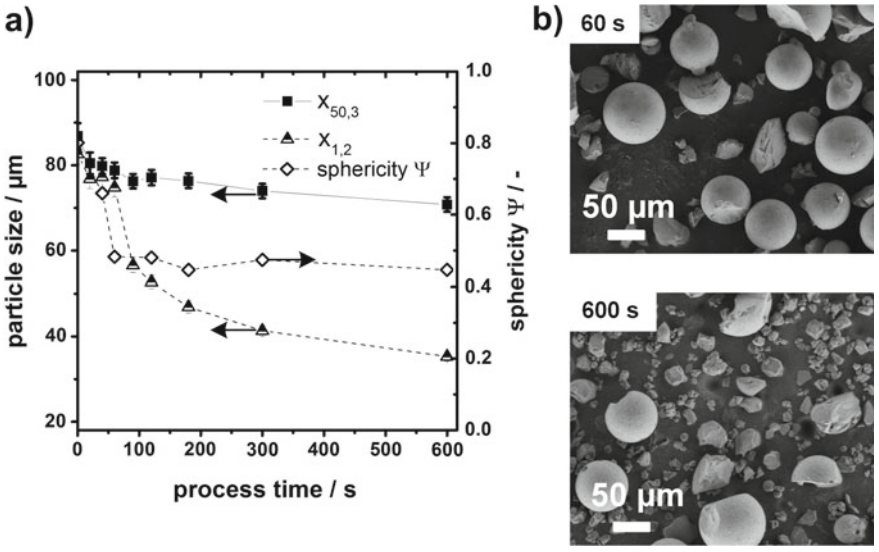

Fig. 5 **a** Change of particle sizes $x_{1,2}$, $x_{50,3}$ and sphericity during batch grinding. **b** SEM images for a feed particle size of $x_{1,2}$ = 93 µm and a holdup of 400 g after 60 and 600 s. Adapted from Köninger et al. [29], with kind permission of Elsevier

processing times (1 min, top image), the number of unbroken feed particles is still high. After 10 min of processing (lower image) mainly fragments dominate.

The few remaining, almost intact particles exhibit dents on the surface. As such, the dent formation is seen as an alternate process to chipping, which causes rather fine fragments. These observations indicate that the feed material is not likely to be broken by one high energy impact but rather by a higher number of impacts producing small fragments. The impacts leading to these small fragments are associated with a high number of impact events at rather low impact velocities. Moderate particle velocities in high-speed gas jets that were injected into fluidized beds were also found by Köninger et al. [34] by particle image velocimetry.

Schönert [42] and later Salman et al. [43] quantitatively characterized the morphological changes of glass spheres after impaction on a target: Different fracture and deformation modes have been assigned to the appearing morphologies whereby each category corresponds to a specific range of the applied mass-specific kinetic energy $W_{m,kin}$. To get a first impression of the grinding conditions in the milling chamber, the method introduced by Salman et al. [43] was applied to the samples in the first 60 s of the quasi-batch grinding experiment. For this purpose the morphology of the particles and fragments is divided into four different types: unstressed immaculate particles (no fracture, smooth surface), particles with low energy impact marks (chipping, dents), fragments showing Hertzian cone cracking, and high impact velocity fragments (appearing as hemispheres, high velocity form). In Fig. 6a examples of the different stressing modes are depicted. In case a particle or fragment could be

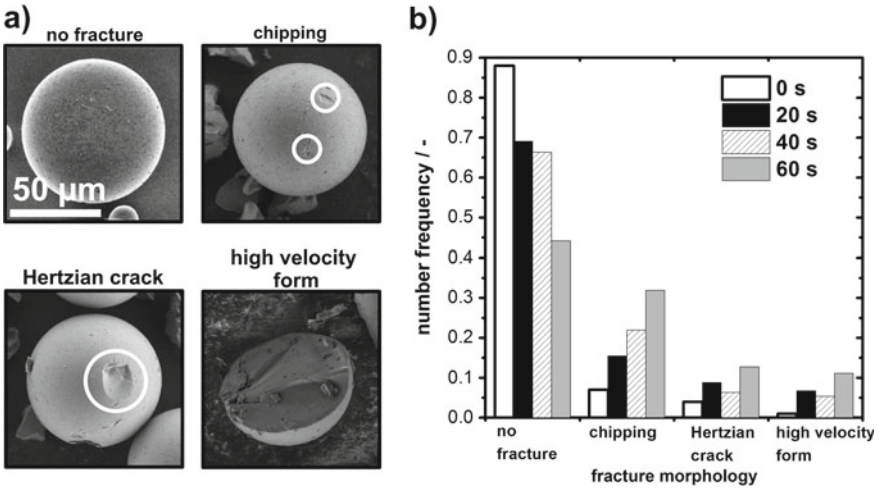

Fig. 6 **a** Four different fracture (respectively impact velocity) categories. **b** Number frequency of the different failure modes after 20, 40 and 60 s of processing. Starting conditions: $x_{1,2} = 93$ µm and a holdup of 400 g. Adapted from Köninger et al. [29], with kind permission of Elsevier

assigned to different classes, the particle was assigned to the class with higher associated impact energy. A minimum of 200 particles was evaluated per sample. The number frequency of the four categories was determined according to Eq. 5:

$$number\ frequency = \frac{number\ of\ particles\ with\ specific\ morphology\ type}{number\ of\ all\ evaluated\ particles} \tag{5}$$

Figure 6b shows the fracture modes for the quasi-batch grinding experiment after processing for 20, 40, and 60 s: Within the first 40 s over 85% of the particles remained unstressed or only traces of a low energy impact (chipping) are visible. Only 5–7% of the spheres could be assigned to the highest impact class. After 60 s the number of particles without visible damage drops significantly, whereas the proportion of particles with several low energy marks on the surface, and particles which have experienced a high-energy stress event (Hertzian cracks and high velocity form), increases. All these observations are in good agreement with the observed trend in Fig. 5. These results already suggest that lower grinding energies are dominant (e.g., in the jet perimeter) and, therefore rather surprisingly, the impact frequency is an essential driving force in fine grinding, if not the most important one. After 60 s a reasonable evaluation of the morphology is impossible due to the high amount of created fines (represented by $x_{1,2}$ in Fig. 5).

However, this method gives no explicit values for the number of impacts and the impact velocity. To target these values more precisely, a technique initially introduced by Peukert and co-workers to characterize the stressing conditions in wet operated stirred media mills [44–46] was adapted: The morphological changes of spherical, well-characterized ductile metal particles are related to the relative particle impact velocities prior to impact. Additionally, the exact number of dents on the particle surface gives information about the stressing frequency. This method will be presented in detail in Sect. 3.3.

3.1.2 Modelling Grinding Kinetics

An excellent approach to modelling grinding kinetics—as proposed by Berthiaux and Dodds [19]—is Kapur's model for batch grinding [47], which is a simple measure for the overall comminution process. Equation 6 gives the particle size-dependent Kapur function $K^{(1)}(x)$, which describes the change of mass within a specific particle size range:

$$\ln\left(\frac{1 - Q_3(x,t)}{1 - Q_3(x,t=0)}\right) = K^{(1)}(x) \cdot t \tag{6}$$

Equation 6 can be used to directly estimate size-dependent breakage rates from the measured PSDs for short comminution times (approximately 80 s): Only small amounts of solid are discharged from the milling chamber during this time interval,

while the process behaves like a batch experiment. These assumptions are only valid for a time-independent breakage rate $K^{(1)}(x)$ and when no nonlinear effects occur [48]. The discharged mass $m_{p,t}$ can be taken into account by adapting the PSD $(1 - Q_3(x, t))$:

$$1 - Q_3(x,t) = \frac{m_{m,t}}{m_{m,t=0}}(1 - Q_3(x,t))_m + \frac{m_{p,t}}{m_{m,t=0}}(1 - Q_3(x,t))_p \tag{7}$$

In Eq. 7 $m_{m,t}$ denotes to the mass inside the milling chamber and $m_{p,t}$ to the total discharged mass at the process time t. Additionally, the mass load at $t = 0$, which is indicated by the same index, is taken as a reference. By using Eq. 7, the Kapur function $K^{(1)}(x)$ from Eq. 6 can be calculated. As already stated, within the first 80 s a linear decrease of the particle size (see Fig. 5a) is observed. The Kapur function was calculated accordingly. The Kapur functions for different holdups of 100, 300, 400, and 700 g (same feed material, $x_{1,2} = 93$ µm) and different initial particle sizes ($x_{1,2}$ = 61, 93, and 127 µm, holdup of 400 g) are shown in Fig. 7. The grinding constant $K^{(1)}(x)$ is plotted against the particle size class: The faster the comminution process within a particle size class, the more negative the values become. For holdups of 100 and 700 g no local extremum is observed, i.e. grinding kinetics increase with the particle size. For medium holdups (300 and 400 g) the fastest grinding kinetics are found in the range of a Sauter diameter of 60–90 µm. Targeting the breakage of particles in the size range between 50 and 90 µm, the corresponding optimum holdup is found between 300 and 500 g: Here, the lowest value of $K^{(1)}(x)$ is observed.

For a load of 100 g, the probability of particle impacts is considered rather low due to the low solid concentration. These low impact probabilities lead to longer path lengths for acceleration before the particles impact with each other. The low holdup corresponds to high kinetic energies per unit mass. A holdup of 700 g is the

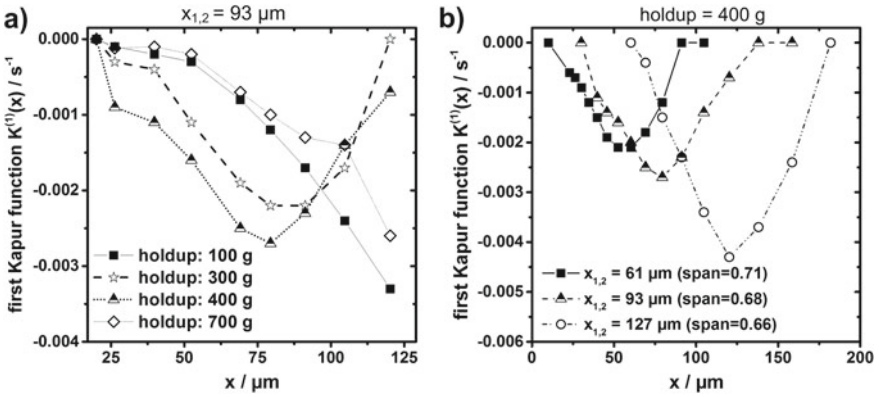

Fig. 7 **a** Kapur function $K^{(1)}(x)$ after 80 s for different holdups with feed particle size $x_{1,2} = 93$ µm and for different feed particle sizes with an initial holdup of 400 g (**b**). Adapted from Köninger et al. [29], with kind permission of Elsevier

other extreme case: the bed height is above the nozzles and back mixing of small particles might be decreased. Due to the high mass concentration, impacts are more likely to happen after shorter acceleration times, whereas the impact probability is comparatively high. For an intermediate holdup of 300 g, the nozzles are covered and the best trade-off between acceleration path lengths and stressing probability is found.

Figure 7b shows the influence of the feed particle size on the Kapur function for an initial holdup of 400 g: For all tested feed materials, a maximum in the grinding kinetics is observed for sizes close to the Sauter mean diameter of the individual fraction. The determined maximum comminution efficiency increases with the particle size. For smaller particles, the entrainment into the jet and the pneumatic transport from the grinding zone is promoted, whereas large particles experience less acceleration inside the jets. Therefore, a higher number of larger particles around the jets is expected which result in an increased impact probability. As will be shown later in Sect. 3.6, the breakage probability is increased for larger particles.

3.2 Fed-Batch Comminution

A changing holdup has a significant influence on the grinding performance of the mill for larger process times. Therefore, the holdup is now kept constant to eliminate this influencing variable. Thus, fed-batch experiments were performed to simulate a constant holdup: During sampling, feed material was added to replace the discharged product. In Fig. 8a $x_{50,3}$ in the milling chamber is shown for different holdups. Similar to the results from the quasi-batch experiments, during the whole process (40 min) no constant particle size is reached. When looking at $x_{50,3}$ for the discharged product, no difference between the holdups was observed. In general, the trend for the discharged fines was found to be similar for the quasi-batch experiment with different holdups shown in Fig. 5a. An increased holdup leads to a faster size reduction of the largest particles in the mill: For more particles being stressed in the active grinding zone, a larger amount of smaller sized fragments is produced. As stated by Fukanaka, comminution is faster at lower holdups due to an increased grinding energy per unit mass [36]. When increasing the pressure and thus the jet speed, an excess of available energy may exist: By increasing the holdup again, the number of impacts inside the jets increases and a faster comminution results. For an increased amount of fines inside the milling chamber, the overall flowability of the solid is decreasing due to agglomeration and adhesion. In consequence, the fluidization behaviour and with it the two-phase flow inside the jets changes. However, this affects the stressing conditions of the particles. Figure 8c gives the discharged product mass flow. The observations are in agreement with Fukanaka: Initially, the mass flow rate is rapidly increasing until reaching a maximum value followed by a steady-state phase. For higher holdups, the time until a steady product mass flow is reached increases. The

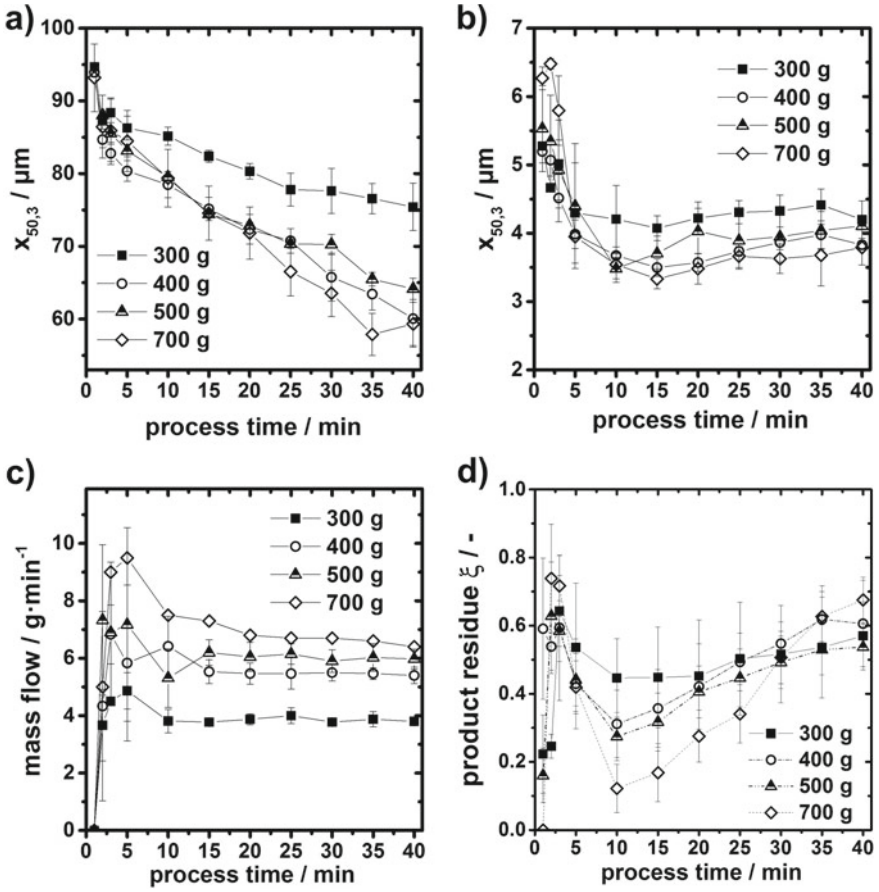

Fig. 8 **a** Particle size $x_{50,3}$ in the milling chamber, **b** $x_{50,3}$ of the discharged product, **c** product mass flow rate, **d** fines residue inside the milling chamber. Data for fed-batch experiments with varying initial holdups. Adapted from Köninger et al. [29], with kind permission of Elsevier

residence time was calculated by dividing the product mass flow rate by the initial holdup. From the product mass leaving the mill during 40 min of processing, residence times between ~75 min (100 g) and ~110 min (700 g) can be calculated for holdups of 100 g and 700 g, respectively. Since the number of impacts strongly correlates with the holdup, the number of impacts increases with increasing residence time.

Within the first 10 min, coarser product particles leave the mill until the steady-state is reached (Fig. 8b). This time was found for all different holdups. A similar observation was made for the corresponding mass flow rates. Independent of the continuously changing fluid mechanical behaviour, which is caused by the decreasing

mean particle size, a stationary product flow rate is reached. Typically, the product fineness and output is sensitive to decreasing particle sizes. However, size-dependent particle pre-separation in the transport zone could minimize that effect on the classifier [49]. Since the various holdups result in different product mass flow rates, a crucial role must be attributed to the load at the classifier and, thus, to the whole process.

Since there is no perfect separation in technical applications, always a certain amount of product-sized particles remains in the coarse fraction. According to Altun and Benzer [50], the effect of fine particles by-passing the classifier and re-entering the circulation system is influenced by the solid concentration. In comparison to stand-alone classifiers, where the rejected material is entering the coarse fraction, the fines are recirculated until they leave the classifier mill. Thus, the product particles re-enter the transport and classification section, before approaching the classifier again. The classifier is therefore exposed to a continuous stream consisting of fresh, crushed and rejected material. Hence, product-sized particles are accumulated inside the milling chamber. The relative amount of product-sized particles which remain inside the milling chamber can be expressed by the product residue ξ (Eq. 8).

$$\xi = 1 - \frac{m_p}{m_m \cdot Q_{3,m}\left(x = x_{90,p}\right) + m_p} \tag{8}$$

The $x_{90,3}$-value of the discharged product is used as threshold diameter for the product particles inside the milling chamber. This approach allows comparing the product discharge process for different holdups—even if the particle size distributions inside the mill differ and the separation curves are unknown. For no accumulation of product-size particles happening inside the milling chamber, ξ should be zero, i.e., all product particles are discharged immediately. Figure 8d gives the product residue ξ as a function of the process time for different holdups. Within the first minutes, most of the product remains inside the mill, despite relatively coarse material being discharged (Fig. 8b). Once the products' target-fineness is reached at approximately 10 min, a minimum in ξ is observed. Despite the now reached stationary product discharge, further grinding again increases the accumulation of the product particles inside the mill.

Regarding the minimum ξ, a higher holdup is beneficial. However, with the ongoing grinding process accompanied by the faster production of fines, the product residue ξ becomes worse for higher holdups. Please note that the product residue is not in a steady state after 40 min of processing since the particle size and with it, the amount of fines inside the milling chamber keeps changing.

3.3 Characterization of Stressing Conditions

3.3.1 Method Development

In general, grinding must be understood by the mill function and the material function. The mill function describes the type of stressing, the transferred stress energy, and the stress number. The material function accounts for the particles' reaction to the applied stress in form of breakage probability and breakage function, i.e. the size distribution of the fragments. For modelling of comminution processes and its grinding kinetics, knowledge about the stressing conditions applied to the particles is essential. To target the impact velocity, i.e. the applied stress energy, and the stressing frequency in the jet mill, a method developed to characterize the stressing conditions in wet operated stirred media mills [45, 46] was adapted: The morphological changes of spherical, well-characterized ductile metal probe particles are related to the relative particle impact velocities prior to impact [33]. Briefly, single particles can be compressed by a flat punch micromanipulator installed in a SEM. Stress-strain curves of several 100 particles can be measured and material properties such as Young's modulus, hardness, yields stress, and absorbed energy can be extracted [51]. The manipulation device in the SEM, also allows to access pictures of the stressed and partly broken particles. Surprisingly, images of compressed silica particles below their brittle-ductile transition (<1 μm) in the SEM and those stressed in a stirred media mill looked very similar, indicating that compression in the SEM mimics compression between two grinding beads. On this basis, the method was initially developed for the case of two-sided stressing in stirred media mills. As probe particles, ductile metal particles are used which do not break but plastically deform. The deformation is a measure of the absorbed energy and thus can be used to extract the kinetic energy of the milling beads. This approach provides the stress energy distribution acting in the mill. Fundamental background information and details of the methodical procedure are reported in two publications of Peukert et al. [45, 46].

In comparison to the method for stirred media mills, a mixture of soda-lime glass beads and aluminium beads was used with a radio of 19:1 m/m. As can be seen in Fig. 3a the two PSDs match perfectly. Since the two materials have a similar density, separation during the comminution process is prevented. As shown earlier, almost no fracture of the glass beads occurs during the first 20 s of the comminution process. The absence of small fragments is essential for the method since they might penetrate into the surface of the softer aluminium particles. Thus, the evaluation of the formed dents would not be possible.

To determine the material parameters for the FEM material's model for the aluminium spheres, single particle impact experiments with 6 mm aluminium spheres against a steel plate were performed. In total, 108 particles were impacted in the velocity range between 10 and 60 m s^{-1}. The obtained correlation (orange dotted line in Fig. 9a) between the velocity v prior to the impact and the resulting contact ratio x_c/x was fitted in a FEM model: Results are depicted in Fig. 9a by the blue

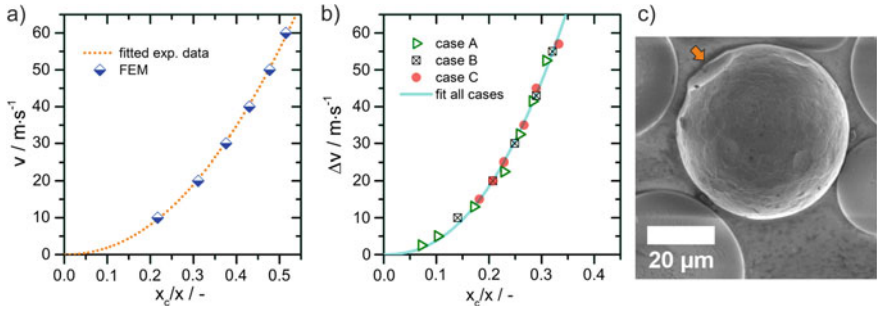

Fig. 9 **a** Fitted experimental data for 6 mm aluminium spheres impacted on a steel plate, impact velocities against normalized contact size x_c/x. **b** Adjusted FEM for different impact cases, relative impact velocities against normalized contact size x_c/x. Case A: "Only one sphere is moving"; case B: "Unidirectional moving of both spheres"; case C: "Head-on collision of both spheres". **c** SEM image of stressed particle (400 g hold-up, 3 bar, $v_{cl} = 32.7$ m s^{-1}). Adapted from Strobel et al. [33], with kind permission of Elsevier

squares (semi-filled, rotated). The fitting procedure resulted in a yield strength and tangent modulus of 95 MPa and 50 MPa, respectively. To ensure similar deformation behaviour of both, the 6 mm and 53.8 µm aluminium spheres, experiments in the impact device of Schönert have been conducted. Almost identical deformation behaviour could be confirmed. The material data of the impacted 6 mm aluminium spheres can thus be used in the next step to simulate particle-particle impact behaviour in the mill.

Figure 9b shows the results from FEM modelling of the particle-particle impact scenario: Since both particles are moving prior to the impact, the relative particle impact velocity Δv is considered. The data for the different impact scenarios "only one sphere is moving" (green triangle, hollow, case A), "unidirectional moving of both spheres" (black square, hollow, crossed-out, case B) and "head-on collision of both spheres" (red circle, full, case C) does not deviate. An exemplary SEM image of an aluminium particle stressed in the fluidized bed opposed jet mill (Fig. 9c) shows the formation of spherical dents on the surface. The glass beads are only elastically deformed; no visible breakage occurred throughout the experiment. FEM simulations indicate that the normalized contact area diameter x_c/x scales with the relative velocity prior to the impact (normal to the particles' surfaces). To account for foreshortening (distortion due to tilted surfaces) Feret diameters of the contact areas were used to determine the contact area diameter x_c.

The stress frequency was addressed by counting the number of dents on the probe particles. The proportion of particles with i contacts $P_i = N_i/N$ (N_i: number of particles with i contacts, N: total number of evaluated particles) is used for calculating the stress numbers $SN_{\%}$ (Eq. 9) and SN_{stress} (Eq. 10).

$$SN_{\%} = 1 - P_0 \tag{9}$$

$$SN_{stress} = \frac{\sum_{i=1}^{n} P_i \cdot i}{1 - P_0} \tag{10}$$

$SN_{\%}$ provides the overall percentage of stressed particles, while SN_{stress} gives the average contact number per stressed particle. For each sample, the contact areas on the visible hemispheres of 100 aluminium particles were evaluated.

3.3.2 Particle Impact Velocity and Contact Numbers

Temporal Evolution

Experiments were performed in the described lab-scaled fluidized bed jet mill for process times of up to 40 min. Figure 10a shows the obtained temporal evolution of the stress number distributions. The overall profile of the curve is maintained while it shifts constantly throughout the process. No fracture of the glass particles was observed during the whole process.

$SN_{\%}$ and SN_{stress} are given in Fig. 10c. After 20 min $SN_{\%}$ approaches 1, i.e. all probe particles have been stressed at least once. Throughout the process, SN_{stress} increases almost linearly. After 40 min an average of eleven contacts per particle was found. The average contact number increases linearly with time, multiple stressing of an existing contact on the probe particles' surface can be excluded. The characteristic shapes of dents on the surface is depicted in Fig. 10d. Further, the distributions of the impact velocity normal to the surface (Fig. 10b) are of similar shape for all investigated processing times. A large number (~90%) of all impacts happens at relative velocities between 6.8 and 9.1 m s^{-1}, respectively. For some impact events, impact velocities of up to 25 m s^{-1} could be found. Remarkably, particle stressing in a single jet occurs at impact velocities significantly lower than the pre-set jet velocity. These surprising and important results imply that the current understanding of grinding in fluidized bed opposed jet mills must be revised. High impact energy events are rare, the stress number seems to be much more important than high stress energy. Consequently, attrition and weakening effects may play a more important role than previously anticipated.

The stressing in stirred media mills, in contrast to the here shown results for the comminution in jet mills, shows fewer, but much larger flat contact pairs (the formation of pairs is attributed to the bilateral stressing by compression). After a process time of 10 min in a stirred media mill, we found an average of 2.5 flat contact pairs on the surface [45, 46]. However, the impact velocity of the approaching grinding beads, and, therefore, the introduced energy, was closer to the values expected by common models.

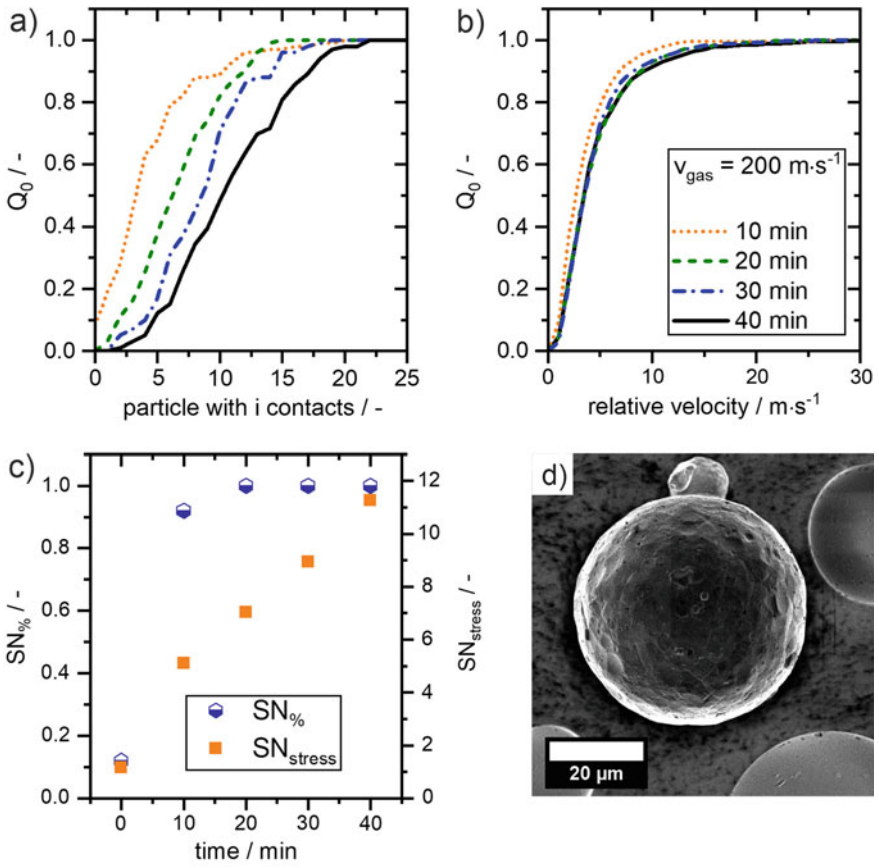

Fig. 10 Number-weighted contact number (**a**) and relative impact velocity distributions (**b**) for different process times in a fluidized bed jet mill (one nozzle). **c** Stress numbers $SN_{\%}$ and SN_{stress} for the respective distributions. **d** SEM image of one probe particle after 40 min. 200 m s^{-1} gas velocity at the nozzle threat. Adapted from Strobel et al. [33], with kind permission of Elsevier

Nozzle Arrangement

The next set of experiments targeted the change in the stressing behavior for two opposing nozzles. Additionally to the increase in number, the distance of the nozzle was systematically varied. Figure 11 again shows the cumulative number-weighted sum distributions for the contacts (a) and the relative velocity (b) for normalized nozzle distances ($z \cdot d_0^{-1}$) of 10 and 21, respectively. As a reference, the corresponding distributions for the single nozzle setup from the previous section are given.

The opposing jet setup shows higher contact numbers (a) and higher relative impact velocities (b) after a processing time of 10 min. The configuration with the

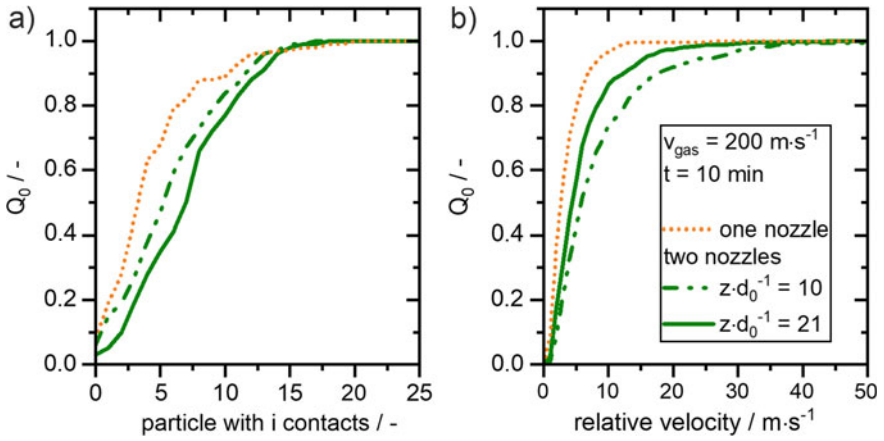

Fig. 11 Cumulative number-weighted sum distributions of the stressing events (**a**) and the relative particle impact velocity (**b**) for different nozzle setups in a fluidized bed reactor with secondary gas injection. Gas velocity of 200 m s^{-1} at the nozzle threat. Adapted from Strobel et al. [33], with kind permission of Elsevier

larger distance between the nozzles ($z \cdot d_0^{-1} = 21$) exhibits the highest number of contacts ($SN_{\%} = 0.97$, $SN_{stress} = 7.6$) as compared to the closer configuration ($z \cdot d_0^{-1} = 10$, $SN_{\%} = 0.94$, $SN_{stress} = 6.6$) and the single jet configuration. Surprisingly, the impact velocities are higher for the smaller nozzle distance. In comparison to the single nozzle setup, the mean velocity of the two nozzle setup is increased by a factor of 1.73 ($z \cdot d_0^{-1} = 21$) and 2.52 ($z \cdot d_0^{-1} = 10$), respectively. We attribute the stress numbers to the differences in the total available jet surface area, i.e. the surface area between the developed jets and the surrounding solid bed. Of course, the surface area is larger for the configuration with the larger nozzle-nozzle distance. However, decreasing the nozzle distance results in a reduced jet boundary area. The single nozzle setup yields the smallest area for particle entrainment, resulting in the lowest overall stress number. We attribute the differences of the relative impact velocities to two factors: Firstly, to the movement of particles in opposite directions, which makes impacts with higher velocities more likely compared to the single nozzle setup, and secondly, to the reduction in the gas velocity due to widening of the jets. The latter effect is more prominent for larger nozzle distances.

Influence of the Holdup

In the following, the above-described method was used to determine the relative particle impact velocity for different holdups [33]: the mills' loading was varied between 100 and 700 g. Grinding pressure was set to 1 bar. Figure 12 shows the results after a processing time of 20 s. This limited process time was chosen due to

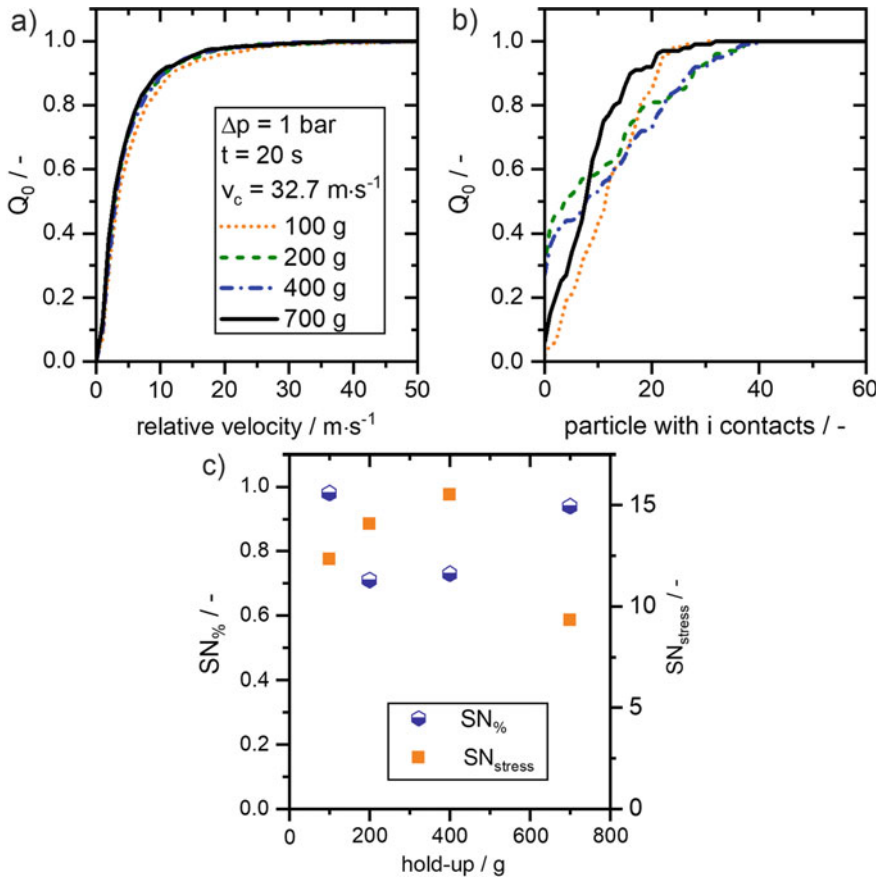

Fig. 12 **a** Relative impact velocity distribution for different holdups in the AFG 100. **b** Number-weighted sum distributions of the contacts on the aluminium probe particles. **c** $SN_{\%}$ and SN_{stress} for the respective distributions. Adapted from Strobel et al. [33], with kind permission of Elsevier

the high number of formed contacts for higher process times. No fracture of the glass beads occurred during this time [52].

Obviously, the relative impact velocity does not depend on the holdup (Fig. 12a): A median impact velocity of approximately 4.8 m s^{-1} was found. Comparing the obtained distributions to the maximum speed in the expanding gas jets, the relative particle impact velocity is significantly lower. However, as Fig. 12b shows, the contact number distributions clearly depend on the hold-up: Looking at the holdups of 100 and 700 g, almost all particles are stressed and show contacts on their surfaces. Further, the number of contacts is higher for the lower holdup. For the holdups of 200 and 400 g, only ~70% of the probe particles show dents. Nonetheless, the stressed probes (200 and 400 g) show the highest number of contacts (see Fig. 12b, c). To gain further insight into the underlying mechanism, the solid distribution inside the mill

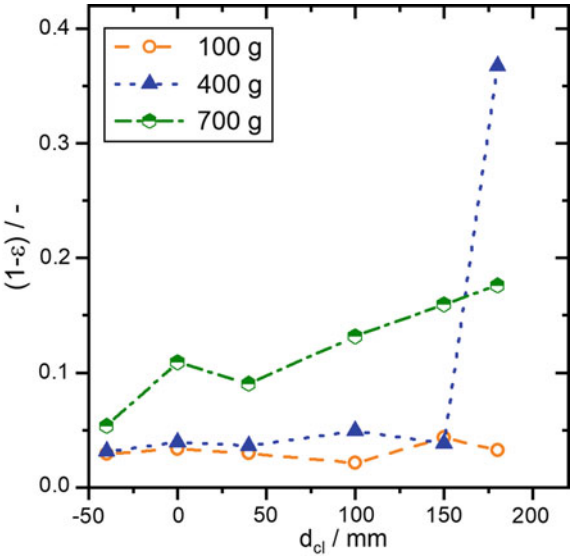

Fig. 13 Solid distribution as function of distance to the classifier for different hold-ups in the AFG 100 accessed by capacitive probes (positive values for the direction of the focal point). Adapted from Strobel et al. [33], with kind permission of Elsevier

was measured by capacitance probes as a function of the distances to the classifier wheel (Fig. 13). The axis of the classifier wheel is used as zero point (positive values for the direction of the focal point). Due to the highly abrasive conditions within the jets, the focal point of the jets is not accessible.

For the lowest holdup, the solid is equally distributed over the whole transport zone. In contrast, for the holdup of 700 g, a linear increase of solids loading towards the grinding zone is visible. For the intermediate holdup of 400 g, the solid concentration measurement indicates a separation inside of the mill: Towards the focal point (high distance) a strongly increased solid concentration was measured (exceeding 35 vol%), while a low solids content (2–5 vol%) was measured for a distance of 150 mm and lower. However, the lower values are comparable to the measured data for a hold-up of 100 g. Thus, the hold-up influences the distribution of the solid content in the grinding chamber during the comminution process: Two compartments with different solid content and a yet unknown mass exchange seem to exist. Therefore, the recirculation inside the mill is crucial for the process. The indications from Fig. 13 are in agreement with previous observations from Sect. 3.1.2: A holdup between 300 and 500 g was found to be most efficient for the comminution of glass beads (yielded the lowest value of $K^{(1)}(x)$ [29]).

Pressure Variation

In the next step, we consider the stress frequency distribution and the stress numbers for a fixed hold-up of 400 g and a grinding pressure of 1, 2 and 3 bar (the rotating speed of the classifier wheel remains constant $v_{cl} = 32.7$ m/s). The results are given

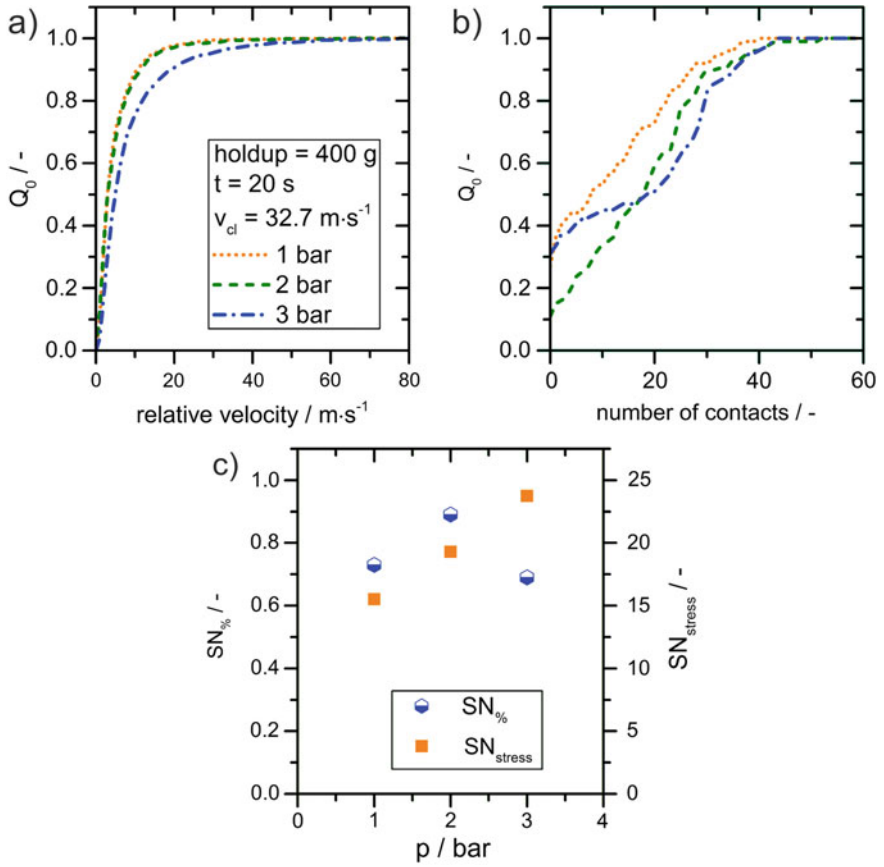

Fig. 14 **a** Relative impact velocity normal to the particle surface. **b** Number-weighted sum distributions of the impact events. **c** Stress numbers $SN_{\%}$ and SN_{stress} (see Eq. **9** and **10**)

in Fig. 14. Obviously, in all cases, the stress numbers are consistently high (Fig. 14c), SN_{stress} lies between 15 and 25). When increasing the pressure to 2 bar, the number of non-stressed probe particles is reduced (Fig. 14b). Increasing the pressure further to 3 bar, a higher number of unstressed particles is observed. Simultaneously, particles with a higher number of contacts appear in the sample. Köninger et al. recently showed for fluidized beds with secondary gas injection, that the solid concentration within the jets decreases upon increasing the gas pressure [34]. Figure 14a shows the influence of the grinding pressure on the relative impact velocity distribution calculated from the measured contact diameters. Between a pressure of 1 and 2 bar only slight differences are visible. At the investigated maximum pressure of 3 bar, the distribution shifts to higher impact velocities. Nonetheless, even at 3 bar maximum impact velocities of 50 m s^{-1} were found only in few cases. However, all median impact velocities ($Q_0 = 0.5$) were smaller than 10 m s^{-1}, a surprising result.

In conclusion, higher grinding pressures lead to higher impact numbers. Accordingly, we attribute the widely observed higher grinding efficiency at higher pressures to a significant increase in the impact numbers rather than to the impact velocity. Considering the approximated residence times from Sect. 3.2 (40 min of processing, feed-batch mode, $x_{1,2} = 93\ \mu m$, between 75 min at 100 g holdup, and 110 min for the 700 g holdup), the influence of the impact number becomes apparent. The number of impacts would add up to several thousand per particle. Considering the high impact numbers and the unexpectedly low relative impact velocities, a fatigue-like behaviour of the stressed particles must be considered as the main driving force of this dry comminution process.

3.4 Transport Zone

For the discharge of the fine solids produced in the grinding zone at the bottom of the grinding chamber, transport to the classifier at the top of the machine is required. Therefore, to participate in the transport, the diameter of the particles must be below the single grain settling diameter in the up-flow: For the used limestone particles the settling diameter was calculated to be ~120 μm [31]. Since already 90% of the initial feed particles are smaller than the single grain settling diameter, the transport of the solids material in the chamber towards the classifier should be promoted. The knowledge of the solid concentration and, therefore, the mass flow towards the classifier is of essential knowledge for the modelling of the apparatus. (Note: For the results discussed in Sects. 3.4 and 3.5, limestone was processed at a grinding pressure of 3 bar in quasi-batch mode. Holdup and classifier speed were changed according to the notifications).

The solid concentration $(1 - \varepsilon)$ in the transport zone (the section between the grinding chamber and the classifier) for different holdups was measured during the comminution process by capacitance probes. Results are shown in Fig. 15a. A linear increase from 0.01 to 0.03 with progressing time is detected for the lowest investigated holdup of 100 g. For the other cases, a maximum in solid concentration is observed right after the start. Besides, the maximum value scales with the initial holdup. With proceeding time, the solid concentration decreases, passes a minimum and rises again, while the differences between the holdups vanish. The rising values following the start indicate an increased production and subsequent transport of fine and intermediate particles towards the classifier. Thus, the load in the transport zone is decreased. Passing the minimum, a significantly higher amount of intermediate particles, which are not discharged but only recirculated in the milling chamber, has to be present. Towards the end of the depicted experiments, the solid concentrations approach a steady-state value. From the processing of glass beads and for the here shown data for limestone, the same overall trend is found: Higher holdups lead to higher solid concentrations in the transport region [29].

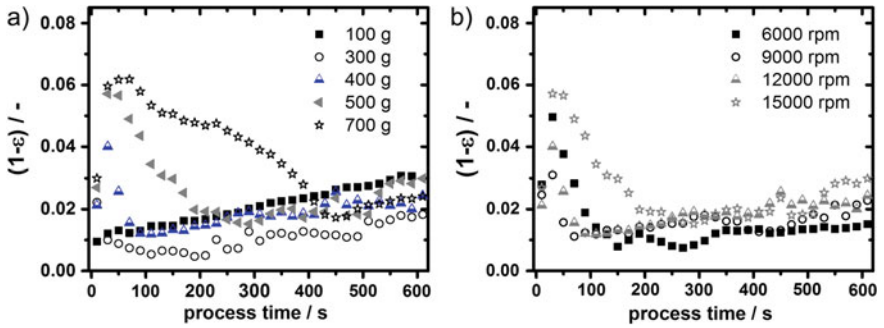

Fig. 15 **a** Solid concentration for different holdups (classifier speed of 12,000 rpm). **b** Solid concentration for different classifier speeds (initial holdup of 400 g). Adapted from Köninger et al. [31], with kind permission of Elsevier

All variations of the classifier speed for a constant initial holdup of 400 g (Fig. 15b) show a similar start-up behaviour with an initial maximum. The time until a steady state is reached increases with the classifier speed. The only exception was found for the lowest classifier speed. Since bigger particles can pass the classifier at smaller circumferential speeds, the range of intermediate-sized particles, that recirculate in the milling chamber and are further stressed, decreases. Accordingly, at 6000 rpm more particles are transported towards the classifier and are discharged.

3.5 Classification

Classification takes place at the upper part of the mill. Fine product particles approach the classifier and are rejected if their diameter is larger than the cut size x_T. Using Eq. 11, which follows from the force equilibrium for a single spherical particle from Stokes law [53], the cut sizes x_T can be estimated. A cut size x_T of 4.4 μm results at a classifier speed of 12,000 rpm.

$$x_T = \sqrt{\frac{18 \cdot v_r \cdot R_{cl} \cdot \eta}{\rho_p \cdot v_{cl}^2}} \tag{11}$$

ρ_p is the particle density, η the dynamic viscosity of the fluid and R_{cl} the radius at the outer classifier blade. As discussed earlier in Sect. 3.2, the discharge of fines during the process changes: Fine product particles are accumulated after a minimum in the product residue ξ is reached for fed-batch experiments. However, for quasi-batch processing of limestone a similar trend was observed, i.e. the product residue changes throughout the whole observation time (see Fig. 16, the cut size is marked by a dotted line).

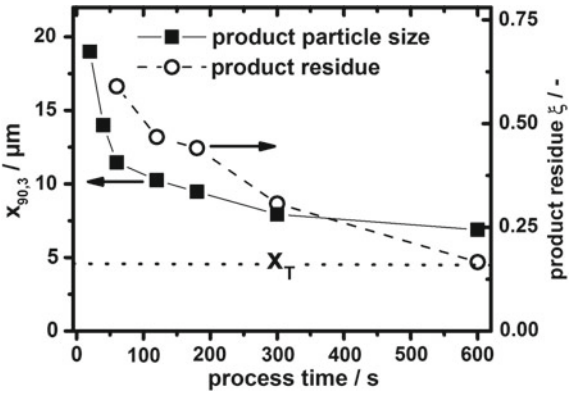

Fig. 16 Product particle size $x_{90,3}$ and product residue ξ inside the milling chamber during quasi-batch grinding with a classifier speed of 12,000 rpm, an initial holdup of 400 g and limestone as feed material. Adapted from Köninger et al. [31], with kind permission of Elsevier

Through the continuously changing size distribution and holdup, the two-phase flow around the classifier changes, too. Further, the rejected particles recirculate in contrast to stand-alone classifiers. Therefore, the determination of separation efficiency curves T(x) is challenging.

Classically, separation efficiency curves relate the mass of particles with the size x which are rejected from a separator to the total mass of particles with the size x fed to the separator. Taking the respective mass flow rates into account, the separation efficiency curve describes the mass flow ratio of particles with the diameter x rejected from the classifier and the particle mass flow with the same diameter x transported to the classifier (Eq. 12). The PSD fed to the classifier is assumed to be equal to the one inside the milling chamber ($q_{3,m}$).

$$T(x,t) = \frac{\dot{m}_{p,t} \cdot q_{3,p}(x,t)}{\dot{m}_{i,t} \cdot q_{3,m}(x,t)} \tag{12}$$

The product mass flow rate $\dot{m}_{p,t}$ and the PSD of the discharged product $q_{3,p}(x, t)$ are directly accessible. The internal mass flow rate transported to the classifier $\dot{m}_{i,t}$ is, however, unknown. An exact calculation of the separation efficiency curve T(x) is thus not possible.

Nonetheless, values for internal mass flow rates have been estimated. Based on the assumption of solely positive values of separation efficiency curves for all particle sizes, the calculated curves after 60 s of processing are plotted in Fig. 17a for values of $\dot{m}_{i,t}$ between 300 and 800 g min^{-1}. Figure 17b displays the estimated efficiency curves after 600 s. $\dot{m}_{i,t}$ was varied between 400 and 1200 g min^{-1}. All separation curves reveal a prominent minimum at approximately 2 µm. This shape of the separation curves is known as "fish-hook". The effect is commonly attributed to the formation of agglomerates and their subsequent rejection at the separator. Thus, fine particles are transferred to the coarse fraction or in our case, are accumulated inside the milling chamber. Relating to the high speed particle tracking results presented later in this section, the observed fish-hooks are attributed to the retaining effect of particle clusters at the periphery of the classifier wheel.

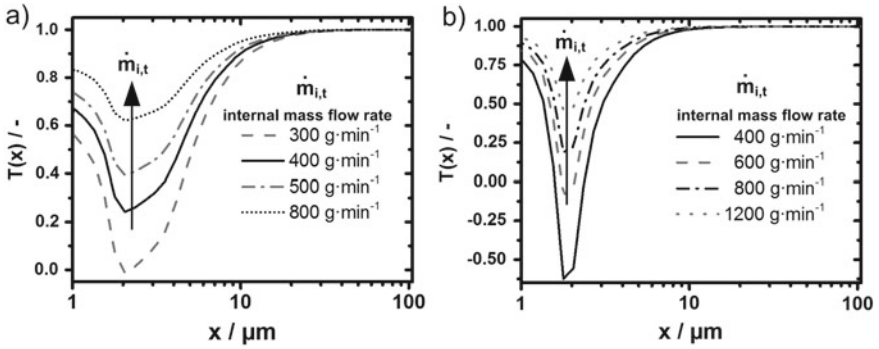

Fig. 17 Separation efficiency curves T(x) after 60 s (**a**) and 600 s (**b**) of processing limestone (3 bar, 400 g initial holdup, 12,000 rpm classifier speed). Different internal mass flow rates were assumed. Adapted from Köninger et al. [31], with kind permission of Elsevier

For a processing time of 60 s a minimum internal mass flow rate of 300 g min^{-1} must be assumed to obtain positive values of the separation efficiency curves, while for 600 s a minimum internal mass flow of at least 400 g min^{-1} needs to be achieved. For internal mass flow rates exceeding the minimum internal mass flow rate, the classification process turns out to be even more ineffective: Due to the ongoing comminution and the associated decrease in particle size, the amount of re-circulating solid increases. Particles impacting on the classifier wheel and thus being broken have been considered as the cause of the partially negative separation efficiency curves. However, from single particle experiments, minimum impact velocities of about 10–20 m s^{-1} to initiate breakage of limestone have been reported [29]. This relative impact velocity of particles at the classifier's blades might only be reached occasionally [32]. Therefore, breakage at the classifier wheel is not likely to happen and can be neglected.

Based on the assumed internal mass flow rates in Fig. 17b, mass loadings at the classifier between 0.265 g g^{-1} (300 g min^{-1}) and 1.05 g g^{-1} (1200 g min^{-1}) result. The differences in operating conditions between classifier mills and stand-alone classifiers are striking: For stand-alone classifiers, mass loadings in the range of 0.1–0.2 are common for fine cut sizes below 10 µm [32, 53, 54].

As explained in the previous sections, the holdup inside the mill influences the internal flow conditions. Obviously, the second influencing variable is the rotational speed of the classifier. When the rotational speed increases, the centrifugal force is rising. Therefore, the discharge of a finer product should be promoted. Further, a broadening of the PSD and an increased residence time should emerge. As displayed in Fig. 18a, the product mass flow increases with decreasing classifier speed during the start-up period of the milling process. Additionally, the ratio of $m_{t=600\ s}$ and $m_{t=0}$, giving the relative amount of solid remaining in the milling chamber after 600 s, is given in Fig. 18a. Only for the highest rotational speeds (12,000 and 15,000 rpm), steady-state conditions are established, whereas the holdup sinks fast for 6000 and

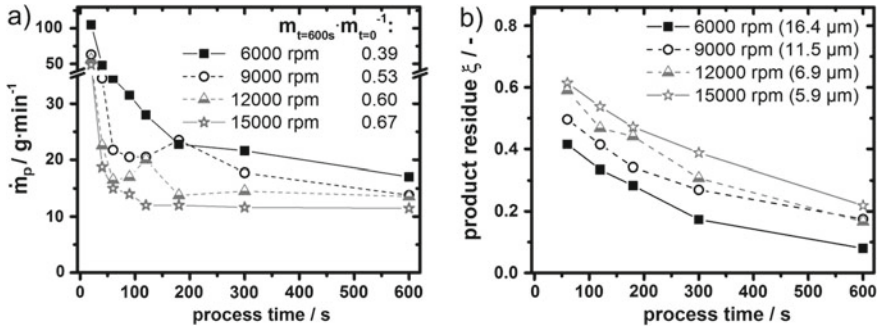

Fig. 18 Product mass flow rates, together with the ratio of $m_{t=600s}$ and $m_{t=0}$, giving the relative amount of solid remaining in the milling chamber after 600 s (**a**) and product residues (**b**) during quasi-batch grinding of limestone for different classifier speeds (initial holdup of 400 g). Adapted from Köninger et al. [31], with kind permission of Elsevier

9000 rpm, respectively. However, the accumulation of fine product is more pronounced for higher centrifugal forces (Fig. 18b). Next to the rotational speed in Fig. 18b, the $x_{90,3}$ values of the discharged product after reaching steady-state conditions are listed: These values indicate that the product accumulation inside the milling chamber is, besides the holdup (explained in Sect. 3.2), a function of the top cut size set by the classifier speed.

Concluding the findings presented so far, a major role can be attributed to the transport and classification process at the classifier and, therefore, has to be considered in greater detail. For that reason, the solid concentration close to the classifier wheel and in its periphery are analysed in the following.

The high-speed images, which have been taken for the visualization of the particle movement, revealed high solid concentrations at the classifier wheel. In the periphery of the classifier wheel, clusters of particles are formed (see Figs. 19 and 20). Particle cluster formation not only takes place at the classifier: As a result of the high solid load inside the mill, clusters can form in the transport zone as well. Even for the lowest investigated holdup of 100 g, the formation of clusters was observed. After a specific time, when solid material is accumulated in the clusters, strands of clusters move tangentially from the outer edge of the classifier wheel to the periphery (see Fig. 19a–c). In Fig. 19d, the cluster frequency, i.e. the number of clusters moving away from the classifying wheel per unit time, is depicted as a function of the classifiers' rotational speed. The observed dependence is in agreement with observations of Spötter et al. [32].

We attribute the previously shown fish-hook effect to the formation of these clusters: Product-sized particles might not be able to penetrate the observed clusters, will be trapped within the clusters, and be thrown back into the periphery. Thus, the discharge of fines from the mill decreases.

With increasing rotational speed and solids holdup, additional clusters are formed in the periphery of the classifier at an outer distance: Two clusters, one at the blade and one in the periphery, are visible in Fig. 20a. The second type of clusters—with

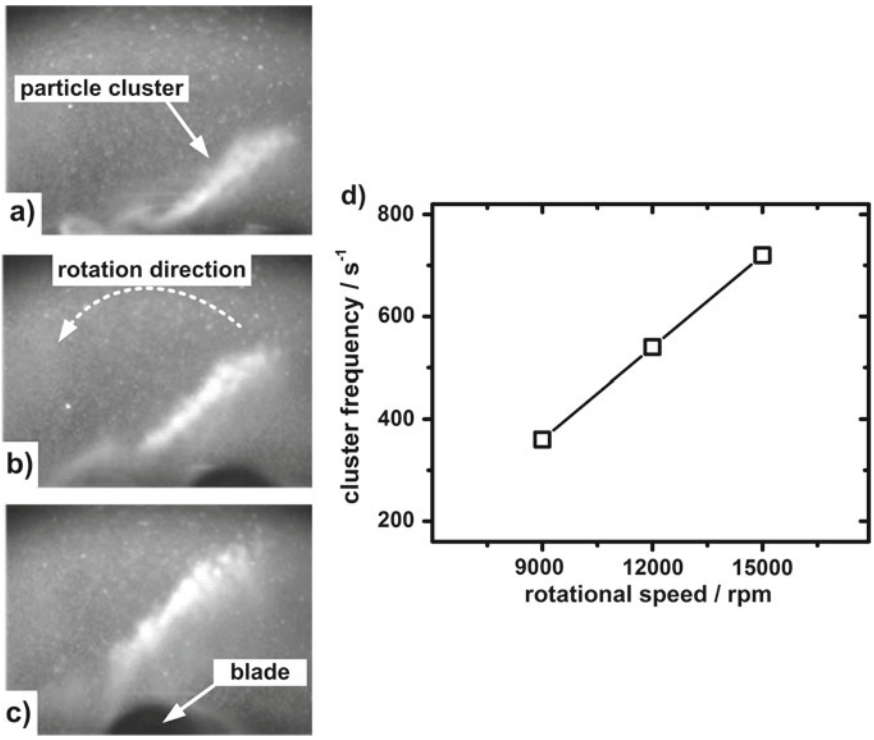

Fig. 19 **a–c** Three consecutive images extracted from high-speed videos [time difference of 3 ms from (**a–c**)]. Movement of a particle cluster away from the outer edge of a classifier blade (100 g initial holdup, 12,000 rpm classifier speed). **d** Cluster formation frequency as a function of the classifier speed (400 g initial holdup). Adapted from Köninger et al. [31], with kind permission of Elsevier

its accumulated particles—rotates in a certain distance to the classifier wheel for some time. Figure 20b–c show three consecutive images of this cluster type. The formed clusters will thus interfere with the solid transport towards the classifier and the following classification process, i.e. they can be seen as scavengers for the fine particles.

Besides the detained fine particles, the clusters mostly consist of intermediate particles, which are too big to pass the classifier, yet are too small to settle and re-enter the grinding zone. The overall amount of clusters increases with increasing holdups [32].

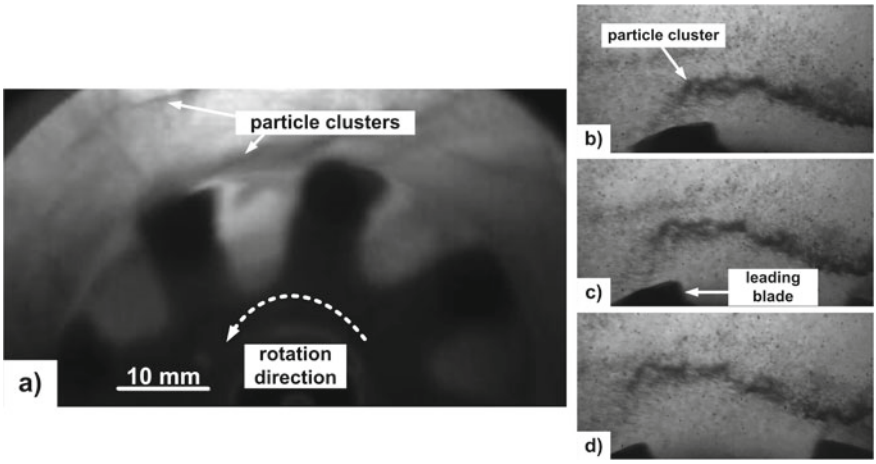

Fig. 20 **a** Particle clusters in the periphery of the classifier wheel (100 g holdup, 12,000 rpm rotational speed). **b–d** Three consecutive images at the outer edge of the classifier [time difference of 3 ms from (**b–d**)], 400 g of holdup, 12,000 rpm rotational speed). Adapted from Köninger et al. [31], with kind permission of Elsevier

3.6 Modelling the Breakage Behaviour

The response of the material to the experienced stress conditions in the mill is the essential part of any grinding model. The stressing conditions are defined in terms of the experienced energy upon impact—in case of jet mills by the impact velocity—and the impact frequency. However, the breakage events in jet mills are not directly accessible due to the highly complex fluid mechanics. In particular, the impact velocities, the impact frequency, and the residence times in the jets are widely distributed. The impact conditions will therefore differ widely: Straight and oblique particle-particle impacts can occur and the impacting particles can be of different size and shape. To model the breakage behaviour of materials, the described Schönert device was used to determine the breakage probability P_B according to the procedure of Vogel and Peukert [39].

Figure 21a shows the measured breakage probability P_B of the previously used glass bead fraction ($x_{1,2} = 93\ \mu m$) given as a function of the number of successive stressing events k, the particle size x, the particles' resistance against breakage f_{mat}, $W_{m,kin}$ and $W_{m,min}$. $W_{m,kin}$ is the mass-specific kinetic energy of the particles prior to the impact, while $W_{m,min}$ is the minimum mass-specific kinetic energy, which resembles a threshold that needs to be exceeded to induce breakage. Therefore, to induce breakage $W_{m,kin}$ needs to exceed $W_{m,min}$. Equation 13 describes the exact relation:

$$P_B = 1 - e^{\{-f_{mat} \cdot x \cdot k \cdot (W_{m,kin} - W_{m,min})\}} \tag{13}$$

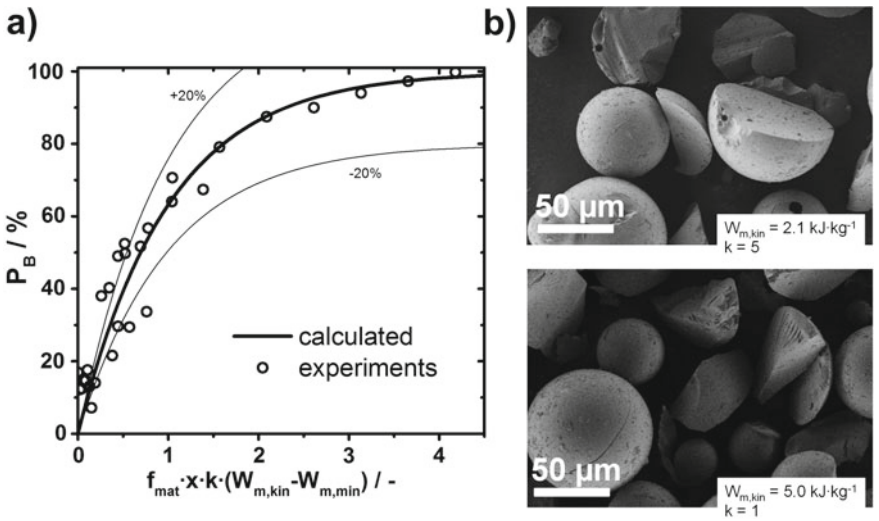

Fig. 21 **a** Breakage probabilities and fitted master curve for the used glass beads ($x_{1,2} = 93$ µm). Material parameters $f_{mat} = 0.944$ kg J m^{-1} and $x \cdot W_{m,min} = 0.1225$ J m kg^{-1} [37]. **b** SEM images of broken particles for different stressing conditions. Adapted from Köninger et al. [29], with kind permission of Elsevier

Impact velocities were in the range of 40–110 m s^{-1} and the number of successive events per particle k was varied between 1 and 8. The shown data points are in good agreement with the master curve. Values for $x \cdot W_{m,min}$ (0.1225 J m kg^{-1}) and f_{mat} (0.944 kg J m^{-1}) are taken from literature [39]. For $W_{m,kin}$ and k being too low, no fragmentation of the particles was observed. Only the formation of rather small dents or cracks on the particles' surfaces was observed. The appearing surface structures are quite similar to the ones from comminution experiments. An insignificant amount of fines is produced. Full fragmentation and a high amount of fines result with increased impact velocity and at a higher number of impacts k. Figure 21b shows the SEM images of two experiments with similar dimensionless stressing parameters $f_{mat} \cdot x \cdot k \cdot (W_{m,kin} - W_{m,min})$ (~0.35) and their degree of fragmentation. The resulting breakage probabilities are quite similar. The particles were stressed one to five times with an energy $W_{m,kin}$ of 2.1 kJ kg^{-1} and 5.0 kJ kg^{-1}, respectively. The breakage function inherently depends on the material properties of the glass beads and on the absorbed energy. Two strategies to increase the breakage probability P_B arise from Eq. 10: Either by increasing the impact velocity and, therefore, the solids kinetic energy $W_{m,kin}$ or by increasing the number of impacts k. The solid concentration influences both cases in the mill.

Low solid concentrations result in longer acceleration distances for the particles in the gas jets before impacting with each other. For higher solid concentrations, the possible acceleration distances decrease dramatically—the particle velocity upon impact is thus reduced. Throughout the process, the particle size x and sphericity ψ change as breakage occurs. As a result, the fluid mechanics is influenced, which then

leads to a higher acceleration a of the particles in the jets.

$$a \sim \frac{F_W}{m_{particle}} \sim \frac{c_w}{x} \tag{14}$$

Equation 14 shows the dependency of the acceleration on the mass-specific drag force $F_W/m_{particle}$, which depends on the drag coefficient c_w and the inverse particle size. From Haider and Levenspiel [55] a relation between the drag coefficient and the sphericity is known:

$$c_w = 69.44 \cdot e^{-5.16\psi} \tag{15}$$

Both during the grinding process and the single particle experiments, the particle size and sphericity decrease. Based on Eq. 15, the drag coefficient will increase with decreasing sphericity. With a continuous increase in the drag coefficient and reduction of the particle size during comminution, the acceleration of the individual particles will increase significantly according to Eq. 14. Thus, the fragmentation process is self-enhancing, at least until intermediate fineness. Since smaller and smaller fragments are produced throughout the process—many of them close to the single-digit micrometre cut size—the impact behaviour of these particles should not be neglected. However, with their increased drag coefficient, the testing should be performed in a reduced pressure environment. These two prerequisites are met by the custom-build low-pressure impact device depicted in Fig. 22. Figure 22a shows the measured velocities for three different fractions of the glass beads ($x_{1,2}$ of 4.7, 17.3, and 60.8 µm). The chamber pressure was set to 100 mbar for all fractions.

The solids mass flow provided by the brush disperser was set to $2.75 \cdot 10^{-5}$ kg s^{-1}. Together with a gas flow rate of $1.6 \cdot 10^{-3}$ m^3 s^{-1}, which enters the acceleration tube through the brush disperser, a solid-to-air flow ratio of $6.8 \cdot 10^{-6}$ was achieved.

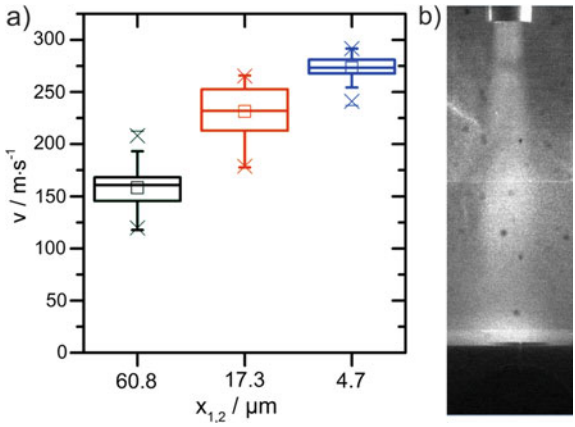

Fig. 22 **a** Box plot of particle velocities for glass bead fractions with different Sauter diameters. **b** Jet inside the impact chamber, visualized by high load of glass beads ($x_{1,2} = 4.7$ µm)

For solid-to-air flow ratios below 0.1 particle-particle interactions are minimized and single impact conditions prevail [56].

Mean velocities of 231 and 274 m s^{-1} were measured for particles with $x_{1,2}$ of 17.3 and 4.7 µm, respectively. The distributions are desirably narrow as indicate by the small boxes. To visualize the behaviour of the particles entering the impact chamber, the solid load was drastically increased. Obviously, turbulences do not interfere with particle impacts on the plate which occur with an angle between 85.8° and 90°. Taking into account the previously determined relative low particle impact velocities (Sect. 3.3.2), product PSDs and morphologies (Sect. 3.1.1), the device provides a sufficient way do determine breakage probabilities for a wide range of materials down to lower micron-size range.

3.7 Modelling Product Mass Flow

Combining all the previously made observations, a simplified model for the product mass flow on the basis of the data for constant mass flow in the jets was introduced by Köninger, based on several assumptions for the boundary conditions: All solids that are added at a particular time step are comminuted. A shift of the particle sizes in the intermediate range is neglected since almost no more changes in the Sauter diameter are observed for process times greater than 40 min. For a constant holdup and PSD in the mill, the product mass flow equals the breakage rate of the added solid material. The breakage rate S is calculated using the breakage probability P_B and the mass flow in the jet area:

$$S = \sum P_{B,i} \cdot \dot{m}_{jet,i} \sim P_B \cdot \dot{m}_{jet} \tag{16}$$

The individual particle classes i and their respective breakage probability $P_{B,i}$ and mass flow in the jet $\dot{m}_{jet,i}$ are neglected. The breakage rate is therefore written as P_B and the solids mass flow in a single jet as $\dot{m}_{jet}$.

For the calculation of the breakage probability (Eq. 13), an averaged value for the impact number k and the particle impact velocity (necessary for $W_{m,kin}$) are used. These averaged values were determined with the particle probe method introduced in Sect. 3.3.1 and applied in Sect. 3.3.2. For a grinding pressure of 5 bar average values of 6.6 m s^{-1} (impact velocity) and 1 s^{-1} (impact rate) were interpolated. Thus, for a residence time of 30 min 1800 impacts are assigned to each particle.

For these stressing conditions, a simplifying assumption for the breakage probability was made: As the average impact velocities from particle probe measurements are far below the minimum impact velocity of approximately 40 m s^{-1}, the minimum mass-specific energy input $W_{m,min}$ is set to 0. If this would be not the case, P_B would vanish and no comminution would happen. We see the assumption $W_{m,min}$ close to 0 indeed as justified based on the observations reported earlier: Image analysis of the broken material and the detected high contact numbers prompted the role of abrasive

effects as one of the primary causes for size reduction. Thus, despite the relatively low impact velocities, comminution can take place. For $k \gg 1$ comminution at any given velocity will take place, and $W_{m,min} \sim 0$ holds true. The energy from these impacts with rather low energy adds up to an overall energy input, which, in consequence, is sufficient to induce breakage of the particle.

The breakage probability P_B of Vogel and Peukert (Eq. 13) can be expanded through a Taylor series (Eq. 17).

$$e^y = 1 + y + \frac{y^2}{2} + \ldots \tag{17}$$

Hence, we assume that the breakage probability is rather low, which is valid for the low impact velocities. A low breakage probability corresponds to low abscissas. Thus, the series expansion is terminated after the second term.

$$e^y = 1 + y \tag{18}$$

In consequence the breakage probability can be expressed as:

$$P_B = \frac{\Delta m_i}{m_{i,0}} = 1 - 1 - y = f_{mat} \cdot x \cdot k \cdot \left(W_{m,kin} - W_{m,\min}\right) \tag{19}$$

With $y = f_{mat} \cdot x \cdot k \cdot \left(W_{m,kin} - W_{m,\min}\right)$.

Taking the solids mass flow in the jet and the discharged product mass flow into account, Eq. (20) evolves:

$$P_B = \frac{\dot{m}_p}{\dot{m}_{jet}} = f_{mat} \cdot x \cdot k \cdot \left(W_{m,kin} - W_{m,\min}\right) \tag{20}$$

Equation 20 can be rearranged for the product mass flow for the jet, which is proportional to the breakage rate S:

$$S \sim \dot{m}_p = f_{mat} \cdot x \cdot k \cdot \left(W_{m,kin} - W_{m,\min}\right) \cdot \dot{m}_{jet} \tag{21}$$

The necessary mass-specific kinetic energy input is calculated using the relative particle impact velocity Δv.

$$W_{m,kin} = \frac{1}{2} \cdot v^2 \tag{22}$$

The solids mass flow in a single jet can be calculated using Eq. 23:

$$\dot{m}_{jet} = \rho_p \cdot (1 - \varepsilon)_{jet} \cdot d_0^2 \cdot \frac{\pi}{2} \cdot u_{p,jet} \tag{23}$$

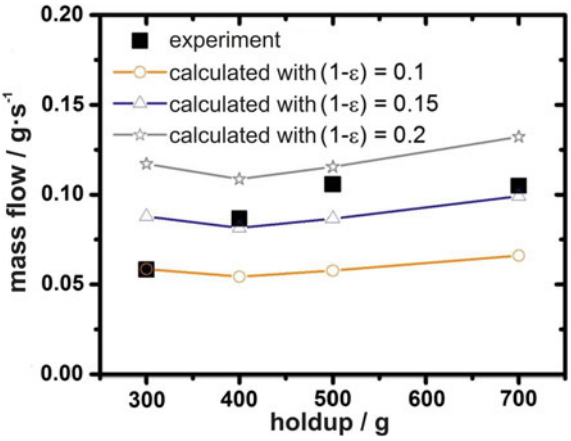

Fig. 23 Stationary product mass flow determined from experiments and approximated according to Eq. 25 for different solid concentrations in the jets (5 bar grinding pressure, 12,500 rpm classifier speed, with kind permission of B. Köninger)

At this point we assume, that the average particle velocity $u_{p,jet}$ in the jet equals the relative particle impact velocity Δv. Inserting Eqs. 22 and 23 into Eq. 21 the following equation results for the breakage rate, respectively the product mass flow.

$$S \sim \dot{m}_p = f_{mat} \cdot x \cdot k \cdot \frac{\pi}{8} \cdot \Delta v^3 \cdot \rho_p \cdot (1 - \varepsilon)_{jet} \cdot d_0^2 \tag{24}$$

For n nozzles in the considered jet mill are used, Eq. 25 results for the overall product mass flow.

$$\dot{m}_p \sim n_{nozzles} \cdot f_{mat} \cdot x \cdot k \cdot \Delta v^3 \cdot \rho_p \cdot (1 - \varepsilon)_{jet} \cdot d_0^2 \tag{25}$$

To calculate the product mass flow according to Eq. 25 a mean solid concentration in the jets is needed. Values between 0.1 and 0.3 are inserted for $(1 - \varepsilon)_{jet}$. As particle diameter $x_{50,3}$ is used, the model gives a trend for different holdups in the fluidized bed opposed jet mill (Fig. 23).

Since the relative particle impact velocity is taken into consideration with a power of 3, a closer look at the impact conditions within the mill is required for further refinements, i.e. by considering both, the whole particle size and impact velocity distribution. The assumptions made for the solid mass flow in the jets together with the breakage model of Vogel and Peukert led to a satisfying first approximation of the product mass flow in fluidized bed opposed jet mills. Moreover, the given equation offers interesting possibilities for the scale-up of these mills, since the diameter d_0 of the used nozzles is taken into account. However, scaling effects concerning the fluid mechanics within the jets need to be examined in greater detail. Köninger varied the nozzle diameter between 1 and 4 mm providing first hints on prevailing correlations.

4 Conclusion

In this chapter, the grinding process in a lab-scale fluidized bed opposed jet mill was investigated. The process and its three different unit operations—namely the comminution in the lower part, the pneumatic transport in the middle section, and the classification step at the top of the mill—were thoroughly discussed. Besides tracking the evolution of the particle sizes in quasi-batch grinding experiments, the morphology of the received fines was discussed. Four different breakage modes could be assigned to the particles from image analysis. The frequency of the cases provides hints on the stressing conditions in the jet mill: In the first minute, most particles exhibit small cracks, small chips and debris are identified, or the particles are unharmed. Larger fragments from high energy impacts were rarely observed.

From grinding kinetics, a medium holdup in the range of 400 g was identified as optimum for the investigated mill size. For larger particles, faster comminution took place. Strong influences of the particle feed size on the final product size could not be observed. Since the holdup influences the grinding kinetics, fed-batch experiments were performed with a constant holdup along the whole process time. In contrast to the quasi-batch experiments, faster comminution was observed for higher holdups in fed-batch mode. However, the accumulation of product particles in the milling chamber strikingly increased towards higher processing times, which led to a more detailed investigation of the classification and transport process.

The presented separation curves showed a fish-hook effect. Product-sized particles accumulated inside the mill for all investigated conditions. For increasing solid holdups and classifier speeds, the amount of accumulated fines increases together with the solid concentration in the transport zone. Additionally, it takes significantly longer for higher holdups to reach a steady state. High-speed images showed the formation of clusters and strands around the classifier: these clusters scavenge fine particles. The fine particles trapped in the cluster are rejected and driven periodically to the outer periphery of the classifier. The formation of clusters at the classifier blades and in the periphery of the classifier wheel is strongly influenced by the classifier speed and solid holdup. Further, the breakage behaviour of the used glass beads was examined by impact testing. The obtained data were in excellent agreement with the breakage model of Vogel and Peukert. For the impact testing of particles below 20 μm, a custom-build low-pressure single particle impact device was designed and operated.

The experimental evaluation of the solid distribution was only addressed for the transport area in the middle section of the mill. However, in addition to the capacitance measurements, the solid distribution in the jet and the surrounding bed was targeted with X-ray tomography. For further information on this method and conducted experiments within this priority program we recommend further works of the authors that are not targeted in this contribution [34, 52].

To gain better insight into the stressing conditions, aluminium particles were used to assess the relative particle impact velocity and stress frequency. The ratio of the formed contact diameter and the particle diameter correlates with the relative particle

impact velocity before the impact. Thus, distributions of the relative particle impact velocity, i.e. of the acting stress energies and stress frequencies in the process were obtained. These experiments clearly confirmed the impression of the breakage modes from SEM images of the glass spheres: A high number of impacts occurs during the process in the mill, while at the same time, the mean relative particle impact velocity is surprisingly low.

Finally, a product mass flow model of Köninger was presented. Based on an adaption of the breakage model of Vogel and Peukert, and using the mean relative particle impact velocity determined by the particle probes, this model provides a reasonable approximation of the experimental data.

Acknowledgements We would like to thank the group of Prof. Weber from TU Clausthal for the fruitful collaboration on classification within the priority program 1679. The support of the Center of Functional Particle Systems is acknowledged as well. The German Research Foundation is acknowledged for funding through the DFG priority program 1679 "Dynamic Simulation of Interconnected Solids Processes".

References

1. Skorych, V., Dosta, M., Hartge, E.-U., Heinrich, S.: Novel system for dynamic flowsheet simulation of solids processes. Powder Technol. **314**, 665–679 (2017)
2. Brosh, T., Kalman, H., Levy, A., Peyron, I., Ricard, F.: DEM–CFD simulation of particle comminution in jet-mill. Powder Technol. **257**, 104–112 (2014)
3. Wheeldon, M., Galk, J., Wirth, K.-E.: Investigation of the comminution process in pendular roller mills. Int. J. Miner. Process. **136**, 26–31 (2015)
4. Ataş, S., Tekir, U., Paksoy, M.A., Çelik, A., Çam, M., Sevgel, T.: Numerical and experimental analysis of pulverized coal mill classifier performance in the Soma B power plant. Fuel Process. Technol. **126**, 441–452 (2014)
5. Rajeswari, M.S.R., Azizli, K.A.M., Hashim, S.F.S., Abdullah, M.K., Mujeebu, M.A., Abdullah, M.Z.: CFD simulation and experimental analysis of flow dynamics and grinding performance of opposed fluidized bed air jet mill. Int. J. Miner. Process. **98**, 94–105 (2011)
6. Toneva, P., Epple, P., Breuer, M., Peukert, W., Wirth, K.-E.: Grinding in an air classifier mill—part I: characterisation of the one-phase flow. Powder Technol. **211**, 19–27 (2011)
7. Weerasekara, N.S., Powell, M.S., Cleary, P.W., Tavares, L.M., Evertsson, M., Morrison, R.D., Quist, J., Carvalho, R.M.: The contribution of DEM to the science of comminution. Powder Technol. **248**, 3–24 (2013)
8. Toneva, P., Peukert, W.: A general approach for the characterization of fragmentation problems. Adv. Powder Technol. **18**, 39–51 (2007)
9. Berthiaux, H., Chiron, C., Dodds, J.: Modelling fine grinding in a fluidized bed opposed jet mill. Powder Technol. **106**, 88–97 (1999)
10. Gommeren, H.J.C., Heitzmann, D.A., Moolenaar, J.A.C., Scarlett, B.: Modelling and control of a jet mill plant. Powder Technol. **108**, 147–154 (2000)
11. Vogel, L., Peukert, W.: Modelling of grinding in an air classifier mill based on a fundamental material function. KONA **21**, 109–120 (2003)
12. Fuerstenau, D.W., Kapur, P.C., De, A.: Modeling breakage kinetics in various dry comminution systems. KONA **21**, 121–132 (2003)
13. Vogel, A.: The Alpine fluidised bed opposed jet mill: a case history. Powder Handling Process. **3**, 129–132 (1991)

14. Lu, X., Liu, C.-C., Zhu, L.-P., Qu, X.-H.: Influence of process parameters on the characteristics of TiAl alloyed powders by fluidized bed jet milling. Powder Technol. **254**, 235–240 (2014)
15. Palaniandy, S., Azizi Mohd Azizli, K., Hussin, H., Fuad Saiyid Hashim, S.: Mechanochemistry of silica on jet milling. J. Mater. Process. Technol. **205**, 119–127 (2008)
16. Schwarzwälder, S., Nied, R., Sickel, H.: Dry fine grinding with jet mills: potentials of energy optimization. Chem. Eng. Technol. **37**, 806–812 (2014)
17. Tasirin, S.M., Geldart, D.: Experimental investigation on fluidized bed jet grinding. Powder Technol. **105**, 337–341 (1999)
18. Wang, Y., Peng, F.: Parameter effects on dry fine pulverization of alumina particles in a fluidized bed opposed jet mill. Powder Technol. **214**, 269–277 (2011)
19. Berthiaux, H., Dodds, J.: Modelling fine grinding in a fluidized bed opposed jet mill. Powder Technol. **106**, 78–87 (1999)
20. Fukunaka, T., Golman, B., Shinohara, K.: Batch grinding kinetics of ethenzamide particles by fluidized-bed jet-milling. Int. J. Pharm. **311**, 89–96 (2006)
21. Xu, X., Li, X., Liu, F., Wei, W., Wang, X., Liu, K., Liu, Z.: Batch grinding kinetics of scrap tire rubber particles in a fluidized-bed jet mill. Powder Technol. **305**, 389–395 (2017)
22. Toneva, P., Wirth, K.-E., Peukert, W.: Grinding in an air classifier mill—part II: characterisation of the two-phase flow. Powder Technol. **211**, 28–37 (2011)
23. Galk, J., Peukert, W., Krahnen, J.: Industrial classification in a new impeller wheel classifier. Powder Technol. **105**, 186–189 (1999)
24. Guo, L., Liu, J., Liu, S., Wang, J.: Velocity measurements and flow field characteristic analyses in a turbo air classifier. Powder Technol. **178**, 10–16 (2007)
25. Liu, R., Zhu, F., Steinberger, Y.: Effectiveness of afforested shrub plantation on ground-active arthropod communities and trophic structure in desertified regions. CATENA **125**, 1–9 (2015)
26. Stender, M., Legenhausen, K., Weber, A.P.: Visualisierung der Partikelbewegung in einem Abweiseradsichter. Chem. Ing. Tec. **87**, 1392–1401 (2015)
27. Sun, Z., Sun, G., Liu, J., Yang, X.: CFD simulation and optimization of the flow field in horizontal turbo air classifiers. Adv. Powder Technol. **28**, 1474–1485 (2017)
28. Xing, W., Wang, Y., Zhang, Y., Yamane, Y., Saga, M., Lu, J., Zhang, H., Jin, Y.: Experimental study on velocity field between two adjacent blades and gas–solid separation of a turbo air classifier. Powder Technol. **286**, 240–245 (2015)
29. Köninger, B., Hensler, T., Romeis, S., Peukert, W., Wirth, K.-E.: Dynamics of fine grinding in a fluidized bed opposed jet mill. Powder Technol. **327**, 346–357 (2018)
30. Richtberg, M., Richter, R., Wirth, K.-E.: Characterization of the flow patterns in a pressurized circulating fluidized bed. Powder Technol. **155**, 145–152 (2005)
31. Köninger, B., Spötter, C., Romeis, S., Weber, A.P., Wirth, K.-E.: Classifier performance during dynamic fine grinding in fluidized bed opposed jet mills. Adv. Powder Technol. **30**, 1678–1686 (2019)
32. Spötter, C., Legenhausen, K., Weber, A.P.: Separation characteristics of a deflector wheel classifier in stationary conditions and at high loadings: new insights by flow visualization. KONA **35**, 172–185 (2018)
33. Strobel, A., Köninger, B., Romeis, S., Schott, F., Wirth, K.-E., Peukert, W.: Assessing stress conditions and impact velocities in fluidized bed opposed jet mills. Particuology, accepted
34. Köninger, B., Hensler, T., Schug, S., Arlt, Wirth, K.-E.: Horizontal secondary gas injection in fluidized beds: solid concentration and velocity in multiphase jets. Powder Technol. **316**, 49–58 (2017)
35. Godet-Morand, L., Chamayou, A., Dodds, J.: Talc grinding in an opposed air jet mill: start-up, product quality and production rate optimization. Powder Technol. **128**, 306–313 (2002)
36. Fukunaka, T., Golman, B., Shinohara, K.: Continuous grinding kinetics of ethenzamide particles by fluidized-bed jet-milling. Drug Dev. Ind. Pharm. **32**, 347–355 (2006)
37. Sigmund Lindner GmbH, Data Sheet. www.sigmund-lindner.com. Accessed 26 June 2017 (2017)
38. Meier, M., John, E., Wieckhusen, D., Wirth, W., Peukert, W.: Influence of mechanical properties on impact fracture: prediction of the milling behaviour of pharmaceutical powders by nanoindentation. Powder Technol. **188**, 301–313 (2009)

39. Vogel, L., Peukert, W.: From single particle impact behaviour to modelling of impact mills. Chem. Eng. Sci. **60**, 5164–5176 (2005)
40. Merkel, M., Thomas, K.-H.: Taschenbuch der Werkstoffe, 7th edn. Fachbuchverlag Leipzig im Carl Hanser Verlag, München (2008)
41. Schittich, C.: Glasbau Atlas, 2nd edn. Birkhäuser, Basel, s.l. (2006)
42. Schönert, K.: Breakage of spheres and circular discs. Powder Technol. **143–144**, 2–18 (2004)
43. Salman, A.D., Gorham, D.A.: The fracture of glass spheres. Powder Technol. **107**, 179–185 (2000)
44. Romeis, S., Schmidt, J., Peukert, W.: Mechanochemical aspects in wet stirred media milling. Int. J. Miner. Process. **156**, 24–31 (2016)
45. Strobel, A., Romeis, S., Wittpahl, S., Herre, P., Schmidt, J., Peukert, W.: Characterization of stressing conditions in mills—a comprehensive research strategy based on well-characterized model particles. Powder Technol. **305**, 652–661 (2017)
46. Strobel, A., Schwenger, J., Wittpahl, S., Schmidt, J., Romeis, S., Peukert, W.: Assessing the influence of viscosity and milling bead size on the stressing conditions in a stirred media mill by single particle probes. Chem. Eng. Res. Des. **136**, 859–869 (2018)
47. Kapur, P.C.: Kinetics of batch grinding: part B. An approximate solution to the grinding equation. Trans. Soc. Min. Eng. AIME **247**, 309–313 (1970)
48. Bilgili, E., Scarlett, B.: Population balance modeling of non-linear effects in milling processes. Powder Technol. **153**, 59–71 (2005)
49. Toneva, P.: Experimentelle und numerische Untersuchungen zur Mehrphasenströmung in Sichtermühlen, 1st edn. Cuvillier Verlag, Göttingen (2010)
50. Altun, O., Benzer, H.: Selection and mathematical modelling of high efficiency air classifiers. Powder Technol. **264**, 1–8 (2014)
51. Paul, J., Romeis, S., Tomas, J., Peukert, W.: A review of models for single particle compression and their application to silica microspheres. Adv. Powder Technol. **25**, 136–153 (2014)
52. Köninger, B., Kögl, T., Hensler, T., Arlt, Wirth, K.-E.: Solid distribution in fluidized and fixed beds with horizontal high speed gas jets. Powder Technol. **336**, 57–69 (2018)
53. Nied, R.: Fine classification with vaned rotors: at the outer edge of the vanes or in the interior vane free area. Int. J. Miner. Process. **74**, S137–S145 (2004)
54. Leschonski, K.: Classification of particles in the submicron range in an impeller wheel air classifier. KONA **14**, 52–60 (1996)
55. Haider, A., Levenspiel, O.: Drag coefficient and terminal velocity of spherical and nonspherical particles. Powder Technol. **58**, 63–70 (1989)
56. Lecoq, O., Chouteau, N., Mebtoul, M., Large, J.-F., Guigon, P.: Fragmentation by high velocity impact on a target: a material grindability test. Powder Technol. **133**, 113–124 (2003)